

THE EVOLUTION TOWARDS ELECTRON-CAPTURE SUPERNOVAE: THE FLAME PROPAGATION AND THE PRE-BOUNCE ELECTRON-NEUTRINO RADIATION

KOH TAKAHASHI,¹ KOHSUKE SUMIYOSHI,² SHOICHI YAMADA,^{3,4} HIDEYUKI UMEDA,⁵ AND TAKASHI YOSHIDA⁵

¹*Argelander-Institut für Astronomie, Universität Bonn, D-53121 Bonn, Germany*

²*Physics Group, Numazu College of Technology, Ooka 3600, Numazu, Shizuoka 410-8501, Japan*

³*School of Advanced Science and Engineering, Waseda University, 3-4-1, Okubo, Shinjuku, Tokyo 169-8555, Japan*

⁴*Advanced Research Institute for Science and Engineering, Waseda University, 3-4-1, Okubo, Shinjuku, Tokyo 169-8555, Japan*

⁵*Department of Astronomy, Graduate School of Science, University of Tokyo, Tokyo 113-0033, Japan*

(Received December 19, 2018; Revised; Accepted)

Submitted to ApJ

ABSTRACT

A critical mass ONe core with a high ignition density is considered to end in gravitational collapse leading to neutron star formation. Being distinct from a Fe core collapse, the final evolution involves combustion flame propagation, in which complex phase transition from ONe elements into the nuclear-statistical-equilibrium (NSE) state takes place. We simulate the core evolution from the O+Ne ignition until the bounce shock penetrates the whole core, using a state-of-the-art 1D Lagrangian neutrino-radiation-hydrodynamic code, in which important nuclear burning, electron capture, and neutrino reactions are taken into account. Special care is also taken in making a stable initial condition by importing the stellar EOS, which is used for the progenitor evolution calculation, and by improving the remapping process. We find that the central ignition leads to intense ν_e radiation with $L_{\nu_e} \gtrsim 10^{51}$ erg s⁻¹ powered by fast electron captures onto NSE isotopes. This pre-bounce ν_e radiation heats the surroundings by the neutrino-electron scattering, which acts as a new driving mechanism of the flame propagation together with the adiabatic contraction. The resulting flame velocity of $\sim 10^8$ cm s⁻¹ will be more than one-order-of-magnitude faster than that of laminar flame driven by heat conduction. We also find that the duration of the pre-bounce ν_e radiation phase depends on the degree of the core hydrostatic/dynamical stability. Therefore, the future detection of the pre-bounce neutrino is important not only to discriminate the ONe core collapse from the Fe core collapse but also to constrain the progenitor hydrodynamical stability.

Keywords: neutrinos — nuclear reactions, nucleosynthesis, abundances — stars: evolution — supernovae: general

1. INTRODUCTION

In a standard theory of stellar evolution, two types of stellar cores have been known to collapse to form a neutron star (NS) (Langer 2012; Janka 2012, for recent review papers). One is a core made of iron-group elements, and the other is a core mainly made of oxygen and neon. A star massive enough to form a Fe core is called a massive star, and the lowest initial mass of the massive star is often indicated by M_{mas} . Because of several theoretical uncertainties including the uncertain efficiency of the convective overshoot, it is difficult to precisely determine the value of M_{mas} , while the current estimates are around 9–11 M_{\odot} for solar-metallicity stars. The ONe core is formed in a super-AGB star, which is less massive than M_{mas} but massive enough to ignite core carbon burning.

Evolution of a collapsing Fe core is relatively well understood (e.g. Arnett 1977; Weaver et al. 1978). A Fe core contracts due to neutrino cooling, electron capture and continuous core mass growth. Core collapse takes place when the instability due to the photo-disintegration sets in at the central part of the Fe core. The collapse lasts until a nascent NS supported by nucleon degeneracy and nuclear repulsive force forms at the center, at which time the bounce shock is created at the core surface and stalls on the way. Although extensive investigations have not yet fully revealed what mechanism(s) accounts for the revival of the stalled shock and how properties of Fe core collapse supernovae (FeCC-SNe) such as the explosion energy are determined, it is widely believed that the core collapse of a Fe core triggers a variety of observed supernovae of type II, Ib, and Ic.

Meanwhile, the evolution of super-AGB star until central oxygen+neon ignition has been investigated in detail by several authors (Garcia-Berro & Iben 1994; Ritossa et al. 1996; Ventura & D’Antona 2005; Siess 2006; Doherty et al. 2010; Lau et al. 2012; Takahashi et al. 2013; Jones et al. 2013; Schwab et al. 2015; and recent review by Doherty et al. 2017). An explosion of so-called electron capture supernova (ECSN) as a result of collapse of a critical mass ONe core has been intensively investigated as well (Hillebrandt et al. 1984; Mayle & Wilson 1988; Kitaura et al. 2006; Dessart et al. 2006; Janka et al. 2008; Fischer et al. 2010; Melson et al. 2015; Radice et al. 2017, including works on accretion induced collapse). However, only a few previous works have studied how the critical ONe core loses its hydrostatic/dynamical stability and reaches core collapse (Miyaji et al. 1980; Nomoto 1987; Takahashi et al. 2013). Accordingly, the late evolution of collapsing ONe cores has not been fully understood.

The distinctive composition of the ONe core complicates the investigations of the last phase of the ONe core evolution: the major components of the ONe core are still combustible. While the Fe core is mainly made of iron group nuclei so that no additional heating due to nuclear reactions is expected, ~ 0.7 MeV per baryon on the average is released through the ^{56}Ni synthesis in the ONe core. As the highly degenerate ONe core typically has a total energy (the sum of the gravitational energy and the internal energy) of $\sim -5 \times 10^{50}$ erg with the core mass of 1.37 M_{\odot} and the core radius of 1.4 R_{\odot} ¹, the available nuclear energy of $\sim 1.8 \times 10^{51}$ erg is enough to explode the entire core, if they burn out instantaneously.

Of course, this simple energy estimate is not enough to determine the fate of the critical mass ONe core because several important nuclear processes take place in the collapsing ONe core. On one hand, the nuclear burning liberates nuclear binding energies increasing the internal energy and the pressure to expand the core. On the other hand, immediately after the nuclear burning, rapid electron capture reactions proceed reducing the internal energy and the electron fraction to accelerate core contraction. Moreover, after the central oxygen+neon ignition, the flame front starts to propagate outward accompanying those important nuclear reactions. Therefore, not only the reactions but also the flame propagation and their interplay must be taken into consideration to understand the hydrodynamic evolution of the critical mass ONe core.

Flame propagation is a successive process, in which nuclear burning recursively takes place at a region just above the front. Therefore, flame propagation can be driven by efficient heat transfer that transports the energy from the hot ash region into the cold fuel region to trigger the subsequent nuclear reactions. And if the front propagation is predominantly powered by a certain mechanism of heat transfer, it is referred to as a deflagration.

So far, heat conduction at the flame front has been considered as a main driving mechanism of the propagation of the deflagration in an ONe core. In this case, heat transfer results from countless energy exchanges by high energy relativistic electrons that travel between the hot and cold regions at a microscopic scale. However, it is difficult to resolve the flame structure in a global simulation, because the length scale of the flame

¹ The degenerate pressure is already relativistic and has a nearly 4/3 adiabatic index. Consequently, the Virial theorem $E_G = -3(\gamma - 1)E_U$ does not agree with $E_G = -1/2E_U$, the limit obtained for the non-relativistic monoatomic ideal gas.

structure of $\sim 10^{-4}$ cm (Timmes & Woosley 1992) is far smaller than the system scale of $\sim 10^8$ cm. Besides, the deflagration velocity in reality may be faster than the one-dimensional laminar flame velocity, when a multi-dimensional corrugation effect on the flame front is considered. Therefore, one needs to apply a certain degree of approximation for the flame propagation in a global simulation of an ONe core, if the flame propagation is driven by the heat conduction.

In the pioneering work by Miyaji et al. (1980), who have investigated the collapse of a critical mass ONe core using a one-dimensional core model composed of oxygen, neon, and magnesium, the propagation has been modeled by setting a simple propagation speed by Nomoto et al. (1976). In a work by Nomoto (1984, 1987) that used a more realistic helium star model and a work by Takahashi et al. (2013) with a full stellar model, the efficiency of the heat transportation by turbulent mixing is estimated using the time-dependent mixing length theory developed by Unno (1967), which reduces the intrinsically multi-dimensional and highly non-linear properties of turbulent mixing into two simple time-differential equations.

While these previous works have found that the ONe core with a high ignition density of $\rho_{\text{ign}} \gtrsim 2.4 \times 10^{10}$ g cm $^{-3}$ finally collapses as a result of efficient energy reduction due to the neutrino radiation and electron reduction due to the electron capture, only the early core collapse before the central densities reach $\rho_c \lesssim 1 \times 10^{11}$ g cm $^{-3}$ has been calculated. In order to consistently describe the core collapse and the succeeding explosion, one needs to follow the evolution up to further high densities ideally until the formation of a nascent NS at $\rho_c \gtrsim 1 \times 10^{14}$ g cm $^{-3}$. The requirements are to incorporate the nuclear EOS as well as to handle complicated interactions between neutrinos and matter.

The purpose of this work is thus to investigate the late evolution of a collapsing ONe core by conducting a hydrodynamical simulation as consistent as possible. The hydrodynamic code used in this work incorporates effects of nuclear burning, electron capture reactions in the nuclear statistical equilibrium (NSE) region, and complicated neutrino transfer as well. We utilize two different progenitor models for the initial condition. In order not to break the hydrostatic structure that the ONe core should initially have, we newly calculate stellar evolution of $9.0 M_{\odot}$ super-AGB star as in Takahashi et al. (2013), which has the ignition density of 1.76×10^{10} g cm $^{-3}$, using the same EOS with the hydrodynamical calculation. Special care has been taken for the remapping process as well. The other progenitor is the model calculated by Nomoto (1984, 1987), which has the ignition

density of 2.4×10^{10} g cm $^{-3}$ and has been widely used as the only progenitor model for ECSNe in the community.

Three limitations exist in this work. The first is omission of electron captures by intermediate-mass elements such as ^{24}Mg and ^{20}Ne . In order to minimize the effect, we use the stellar structure just before the ignition of oxygen and neon as the initial condition for the new progenitor model. The second and third limitations are omissions of heat transfer by heat conduction and of the multi-dimensional effects of turbulence at the flame front. Discussions on these limitations are made in the text.

Apart from the physical limitations, there is a debatable uncertainty in the progenitor evolution. That is, if no effective matter mixing takes place after the initiation of the electron capture on ^{20}Ne , the central temperature suddenly increases and leads to the ignition of the central O+Ne with a low ignition density of $\sim 9 \times 10^9$ g cm $^{-3}$ (Miyaji & Nomoto 1987; Canal et al. 1992; Gutierrez et al. 1996; Schwab et al. 2015). Recent multi-dimensional simulations indicate that explosive mass ejection similar to the thermonuclear explosion can take place with such a low ignition density (Jones et al. 2016; Leung & Nomoto 2017, also see Nomoto & Kondo 1991; Isern et al. 1991). In this context, our progenitor model having the ignition density of 1.76×10^{10} g cm $^{-3}$ would be destined for a core collapse.

The paper is organized as follows. Description of the radiation-hydrodynamic code is given in section 2. We explain the initial conditions in section 3. Results of hydrodynamic calculations are reported in section 4 for the new progenitor model and in section 5 for the Nomoto's progenitor. In section 6, possible contributions of other neutrino reactions to the flame propagation are examined, then the effect of turbulent corrugation to the conductive flame propagation in the ONe core is discussed. Conclusions are drawn in section 7.

2. RADIATION-HYDRODYNAMIC CODE

The explosion is simulated by a 1-D time-implicit Lagrangian general-relativistic radiation-hydrodynamic code (Yamada 1997; Yamada et al. 1999). This code has been utilized to study the Fe core collapse supernovae from core massive stars (Sumiyoshi et al. 2005, 2007, 2008; Nakazato et al. 2007, 2013). The code comprises the approximate Riemann solver by the Roe method. Four flavors of neutrino, electron-, anti-electron, mu/tau-, and anti-mu/tau-neutrino, are considered in this work. The neutrino transport is formulated based on the Boltzmann equation, in which the evolution of the neutrino distribution function in the three-dimensional phase space (mass coordinate \times neu-

trino energy \times azimuth angle from the radial direction) is solved. The mass coordinate is in common with both hydrodynamic and neutrino transfer equations. Resolutions are 511 grid points for the mass coordinate, 14 grid points for the neutrino energy, and 6 grid points for the azimuth angle. Below we describe extensions of the code for the current study.

2.1. Treatment of non-NSE Compositions

In the collapsing phase of the ONe core, nuclear burnings modifies the original non-NSE chemical composition (e.g., oxygen-neon and carbon-oxygen) to achieve the NSE. As a result of the phase transition, the matter entropy increases and a rapid electron capture reaction initiates. In order to properly deal with these phenomena, the evolution of chemical composition is carefully treated in this work.

Two types of equation of states (EOSs) are included in the hydrodynamic code. One is a nuclear EOS based on a relativistic mean field theory (the STOS EOS, Shen et al. 1998). Since reaction equilibrium among baryons is assumed in the nuclear EOS, it is applicable for a region where NSE is realized. For non-NSE regions, a composition-dependent EOS is imported from the stellar code (Takahashi et al. 2016). The stellar EOS consists of ideal gases of radiation, electron and positron, proton, neutron, alpha-particle, and heavy-nuclei. Consistency check between the two EOSs has been done for a wide parameter range, which is provided in Appendix.

The EOS comparison shows that the two EOSs can be smoothly connected if the switching temperature is adequately determined. The switching over the two EOSs in the current work is carried out by a simple temperature-density dependent manner. A transition region is defined in a temperature-density plane by $\Lambda_{\text{trans}} = \Lambda_2 - \Lambda_1$ with $\Lambda_i = \{(T, \rho) | T < T_i, \rho < \rho_i\}$ and $T_1 = 5.80 \times 10^9$ K (= 0.5 MeV) and $T_2 = 9.28 \times 10^9$ K (= 0.8 MeV), and $\rho_1 = 3 \times 10^{12}$ g cm $^{-3}$ and $\rho_2 = 7 \times 10^{13}$ g cm $^{-3}$. A weight function W is defined as

$$W(T, \rho) = \begin{cases} \max\left(\frac{\log T - \log T_1}{\log T_2 - \log T_1}, \frac{\log \rho - \log \rho_1}{\log \rho_2 - \log \rho_1}\right) & ((T, \rho) \in \Lambda_{\text{trans}}) \\ 0 & ((T, \rho) \in \Lambda_1) \\ 1 & (\text{otherwise}), \end{cases} \quad (1)$$

so as to connect zero and unity in the transition region. Using W , a thermodynamic quantity f is calculated as $f = (1 - W)f_{\text{stellar}} + Wf_{\text{STOS}}$, where f_{stellar} or f_{STOS} are quantities derived by each EOS.

Chemical composition in a non-NSE region is described by 49 species of isotopes (Table 1). For a low temperature region of $T < 10^{9.7}$ K, evolution of chemical

Table 1. 49 Isotopes Included in the Hydrodynamic Code

Element	A	Element	A	Element	A
n	1	Ne	20	Ca	40
H	1–3	Na	23	Sc	43
He	3–4	Mg	24	Ti	44
Li	6–7	Al	27	V	47
Be	7, 9	Si	28	Cr	48
B	8–11	P	31	Mn	51
C	12–13	S	32	Fe	52–56
N	13–15	Cl	35	Co	55–56
O	15–18	Ar	36	Ni	56
F	17–19	K	39		

composition is calculated by solving a reaction network,

$$\begin{aligned} \frac{dY_i}{dt} &= \dot{Y}_i(T, \rho, Y_j) & (2) \\ &= -\lambda_{i \rightarrow j} Y_i + \lambda_{j \rightarrow i} Y_j - \sum_{j,k} \lambda_{i \rightarrow jk} Y_i Y_j \\ &\quad + \sum_{j,k} \lambda_{jk \rightarrow i} Y_j Y_k \dots, & (3) \end{aligned}$$

where Y_i is the mole fraction of i th isotope and λ are the reaction rates. Otherwise, chemical-potential-based NSE equations,

$$\mu_{(A,Z)} = Z\mu_p + (A - Z)\mu_n, \quad (4)$$

are solved. Here A and Z are the mass and the proton numbers, and $\mu_{(A,Z)}, \mu_p, \mu_n$ are chemical potentials of (A, Z) isotope, proton, and neutron, respectively. These equations are simultaneously and iteratively solved with other hydrodynamic equations. For this purpose, mole fractions Y_i are added to a set of independent variables in our code.

Note that nuclear weak reactions such as electron captures and beta decays are not treated in the nuclear reaction network but included in the Boltzmann equation. This causes an inconsistency between Y_e calculated by the reaction network, which becomes constant for each mass grid, and that calculated by the Boltzmann equation. We use Y_e determined by the Boltzmann equation for the hydrodynamical calculation. Consistent treatment between the nuclear reaction network and the Boltzmann equation will be done in the future.

2.2. Reaction kernel of the electron-type neutrino absorption on nuclei

The collision term in the Boltzmann equation in this work is composed of 6 nuclear weak reactions and 3 thermal pair emissions (Bruenn 1985; Mezzacappa & Bruenn

1993; Braaten & Segel 1993; Friman & Maxwell 1979; Maxwell 1987; Yamada et al. 1999; Sumiyoshi et al. 2005). Nuclear weak reactions are; electron-type neutrino absorption on neutron (and its inverse reaction); electron-type anti-neutrino absorption on proton (and its inverse reaction); electron-type neutrino absorption on nuclei (and its inverse reaction); neutrino-nucleon scattering; neutrino-electron scattering; and neutrino-nuclei coherent scattering. Thermal pair emissions are; electron-positron pair processes; plasmon processes; and bremsstrahlung. Among them, treatment of the electron-type neutrino absorption on nuclei, or electron capture on nuclei in other words, is improved in the present study.

Emission- and absorption kernels, R^e and R^a , appear in the collision term as

$$\left(e^{-\phi} \frac{\partial f_\nu}{c \partial t} \right)_{\text{coll}} = R^e (1 - f_\nu) - R^a f_\nu, \quad (5)$$

where c is the speed of light, $g_{00} \equiv e^{2\phi}$ is the (0,0) component of the metric, and f_ν is the neutrino distribution function. The absorption kernel is related to the emission kernel as $R^a = \exp(\beta(E_\nu + \mu_n - \mu_p - \mu_e)) R^e$ so as to ensure the detailed balance, where $\beta \equiv 1/kT$ is the inverse of the temperature, E_ν is the energy of the neutrino, and μ_e is the electron chemical potential. To conduct the calculation, the value of the reaction kernels has to be estimated.

So far, the reaction kernel of electron capture on nuclei is formulated for an approximate averaged nuclei (Bruenn 1985). In this work, we instead use the electron capture rate compiled by Furusawa et al. (2017a), in which electron capture reactions on each isotope are considered based on the tabulated and approximated reaction rates and summed up with an NSE chemical composition (for details, see Juodagalvis et al. 2010; Furusawa et al. 2017b,a; Kato et al. 2017). Thus the NSE averaged electron capture rate, $\lambda_{\text{ec}} \equiv -\partial n_e / \partial t$, and the energy distribution of neutrino emitted by electron capture, $\psi_\nu(E_\nu)$, are tabulated as functions of density, temperature, and Y_e . Here, the energy distribution is normalized to be $1 = \int \psi_\nu(E_\nu) dE_\nu$.

Assuming that isotropic neutrino emission takes place by the electron capture, the relation, $\psi_\nu(E_\nu) \propto R^e E_\nu^2$, holds. Also for simplicity, here we assume $f_\nu \ll 1$ and neglect the general relativistic effects. Then the electron capture rate can be equated as

$$\lambda_{\text{ec}} = \frac{\partial n_\nu}{\partial t} \quad (6)$$

$$= \int \frac{1}{(hc)^3} (cR^e) d^3 E_\nu. \quad (7)$$

Since $\psi_\nu(E_\nu)$ is normalized, the emission kernel is equated as

$$R^e = \frac{(hc)^3}{4\pi c E_\nu^2} \lambda_{\text{ec}} \psi_\nu. \quad (8)$$

2.3. Treatment of the entropy equation

Since the ONe core has a low temperature, even a weak heating can significantly change the core entropy and thus the temperature. Physical origins of the heating are nuclear- and neutrino reactions and shock heating. Among them, an indispensable numerical error is often caused by the shock heating. The early evolution of the ONe core is especially susceptible to the numerical heating, and our test calculation shows unphysically fast flame propagation. This is why we have taken special care to treat the entropy equation in the code.

The entropy equation can be formulated with the energy conservation (see discussion in Takahashi et al. 2016, for non-general-relativistic case) as

$$T \frac{\partial s}{\partial t} = \frac{\partial \epsilon}{\partial t} - p \frac{\partial \tau}{\partial t} - \mu_e \frac{\partial Y_e}{\partial t} - \sum_{\text{ion}} \mu_i \frac{\partial Y_i}{\partial t} \quad (9)$$

$$e^{-\phi} \frac{\partial \epsilon}{\partial t} = e^{-\phi} p \frac{\partial \tau}{\partial t} - \tau Q, \quad (10)$$

where T , s , ϵ , p , $\tau \equiv 1/\rho_b$ are the temperature, the specific entropy, the specific internal energy, the pressure, the inverse of the baryon mass density, respectively, and Q is the neutrino energy loss rate (see Yamada 1997; Yamada et al. 1999, for the detailed definitions). With the help of the baryon number conservation and the momentum conservation, the energy equation (eq.(10)) is reformulated to reproduce the Rankin-Hugoniot relation as

$$\begin{aligned} e^{-\phi} \frac{\partial \epsilon}{\partial t} &= \left[e^{-\phi} p \frac{\partial \tau}{\partial t} \right]_{\text{shock}} - \tau Q \quad (11) \\ \left[e^{-\phi} p \frac{\partial \tau}{\partial t} \right]_{\text{shock}} &\equiv -\frac{1}{\Gamma} \frac{\partial}{\partial m} (4\pi r^2 p U) - \frac{h}{\Gamma^2} e^{-\phi} \frac{\partial}{\partial t} \left(\frac{1}{2} U^2 \right) \\ &\quad + \frac{h}{\Gamma^2} \tilde{m} e^{-\phi} \frac{\partial}{\partial t} \left(\frac{1}{r} \right) + \frac{h}{\Gamma^2} 2\pi e^{-\phi} \frac{\partial r^2}{\partial t} (p + p_\nu) \\ &\quad - \frac{1}{\Gamma} \tau U q + \frac{p}{\Gamma} 4\pi r \tau F_\nu, \quad (12) \end{aligned}$$

where Γ , $U \equiv e^{-\phi} \partial r / \partial t$, $h \equiv 1 + \epsilon + p\tau$, \tilde{m} , are the general relativistic gamma factor, the radial fluid velocity, the specific enthalpy, and the gravitational mass, and p_ν , q , F_ν are quantities related to neutrinos, respectively (see Yamada 1997; Yamada et al. 1999, for the detail definitions).

The difference between $e^{-\phi} p \frac{\partial \tau}{\partial t}$ and $\left[e^{-\phi} p \frac{\partial \tau}{\partial t} \right]_{\text{shock}}$ expresses the effect of shock heating. Hence we define

$$\tau Q_{\text{shock}} \equiv \left[e^{-\phi} p \frac{\partial \tau}{\partial t} \right]_{\text{shock}} - e^{-\phi} p \frac{\partial \tau}{\partial t} \quad (13)$$

as the shock heating rate. Accordingly, we reformulate the entropy equation as

$$e^{-\phi}T\frac{\partial s}{\partial t} = -e^{-\phi}\mu_e\frac{\partial Y_e}{\partial t} - e^{-\phi}\sum_{\text{ion}}\mu_i\frac{\partial Y_i}{\partial t} + \tau Q + \tau Q_{\text{shock}} \times i_{\text{shock}}, \quad (14)$$

where i_{shock} is a switching function defined as

$$i_{\text{shock}} = \begin{cases} 1 (s_k > 1) \\ 0 (\text{otherwise}). \end{cases} \quad (15)$$

3. INITIAL CONDITIONS

3.1. Model T9.0

We have calculated a new progenitor model, which hereafter is referred to as the model T9.0. Using a stellar evolution code described in Takahashi et al. (2014), an evolution of a solar metallicity 9.0 M_{\odot} model is calculated from the pre-main-sequence phase until just before the oxygen ignition at the center of the ONe core. A reaction network of 62 isotopes is solved in the evolution code, in which electron capture reactions by ^{20}Ne , ^{20}F , ^{24}Mg , ^{24}Na , ^{23}Na , ^{25}Mg , and ^{27}Al are taken into account. The baryon core mass becomes 1.365 M_{\odot} at the end of the evolution calculation, but is slightly reduced to 1.361 M_{\odot} when the data is mapped onto the hydrodynamic code. The ignition density is 1.76×10^{10} g cm³. The effect of stellar rotation has not been taken into account in this model. The initial structure used in the hydrodynamical calculation is shown in Fig. 1. Quantities every ten grid points are shown by crosses in the figure, showing that grid points are well defined.

Since the evolutionary properties are essentially the same as our previous result (Takahashi et al. 2013), here we briefly describe some modifications in the current calculation method and their consequences.

The description of convective matter mixing has been modified. We solve a diffusion equation to consider the mixing of chemical species. We apply the Ledoux criterion for the convective criterion, i.e., dynamically unstable regions are defined according to the condition

$$\nabla_{\text{rad}} > \nabla_{\text{ad}} + \frac{\varphi}{\delta}\nabla_{\mu}, \quad (16)$$

where $\varphi \equiv (\partial \ln \rho / \partial \ln \mu)_{p,T}$ and $\delta \equiv -(\partial \ln \rho / \partial \ln T)_{p,\mu}$ are thermodynamic functions, $\nabla_{\mu} \equiv d \log \mu / d \log p$ is the μ -gradient, and $\nabla_{\text{rad}} \equiv (\kappa L / 16 \pi c G M)(3P / aT^4)$ and $\nabla_{\text{ad}} \equiv (\partial \ln T / \partial \ln P)_{s_k,\mu}$ are the radiative and adiabatic temperature gradients, respectively. For this region, the diffusion coefficient is determined as

$$D_{\text{conv}} = \frac{1}{3}v_{\text{mix}}l_{\text{mix}}, \quad (17)$$

where v_{mix} and $l_{\text{mix}} = \alpha_{\text{mix}}H_p$ are the velocity and the mixing length of convective blobs determined by the mixing-length theory (Böhm-Vitense 1958). Also the vibrational instability is assumed to grow in a region of

$$\nabla_{\text{ad}} + \frac{\varphi}{\delta}\nabla_{\mu} \geq \nabla_{\text{rad}} > \nabla_{\text{ad}}, \quad (18)$$

and a semi-convective diffusion coefficient of Spruit (1992)

$$D_{\text{sc}} = f_{\text{sc}} \frac{\nabla_{\text{rad}} - \nabla_{\text{ad}}}{(\varphi/\delta)\nabla_{\mu}} D_{\text{therm}}, \quad (19)$$

where $D_{\text{therm}} = (1/c_p\rho)(4acT^3/3\kappa\rho)$ is the thermal diffusivity, is used for the region. The free parameter f_{sc} is set to be $f_{\text{sc}}=0.3$, which result in semi-convective mixing of intermediate strength (Umeda et al. 1999; Umeda & Nomoto 2008). In addition, the effect of convective overshooting is taken into account for core hydrogen and core helium burning stages. An exponentially decaying function (Herwig 2000) is used to determine additional diffusion coefficient from the edge of the convective regions as

$$D_{\text{conv,ov}} = D_{\text{conv,0}} \exp\left(-2\frac{\Delta r}{f_{\text{ov}}H_{p,0}}\right), \quad (20)$$

where f_{ov} is an adjustable parameter, $D_{\text{conv,0}}$ and $H_{p,0}$ are the convective mixing coefficient and the pressure scale height at the edge of the convective region, and Δr is a distance from the edge. Parameters are calibrated to explain the position of the red-giants ($\alpha_{\text{mix}} = 1.5$) and the main-sequence width of stars in open clusters ($f_{\text{ov}} = 0.015$) observed in our galaxy in the HR diagram. A star forms a more massive core as a result of inclusion of the overshooting mixing. This is why the initial mass of the current model has been reduced from 10.4–10.8 M_{\odot} in Takahashi et al. (2013) to 9.0 M_{\odot} .

The evolution calculation has once been halted soon after convective regions in the helium layer and the hydrogen rich envelope have merged (the dredge-out episode, Iben et al. 1997). The further evolution of the degenerate core is calculated by removing the outer region and by setting new boundary conditions. By assuming that fitting with the highly inflated condensed-type envelope (Chandrasekhar 1939) is always achieved at the surface of the core, two relations of

$$0 = \nabla_{\text{rad}} - 1/4 \quad (21)$$

$$0 = 2U + V - 4, \quad (22)$$

are imposed (e.g., Sugimoto & Fujimoto 2000), where $U \equiv 4\pi r^3 \rho / M$, and $V \equiv GM\rho / PR$ are the homologous parameters. This not only gives more physically consistent surface structure of the core, but also improves

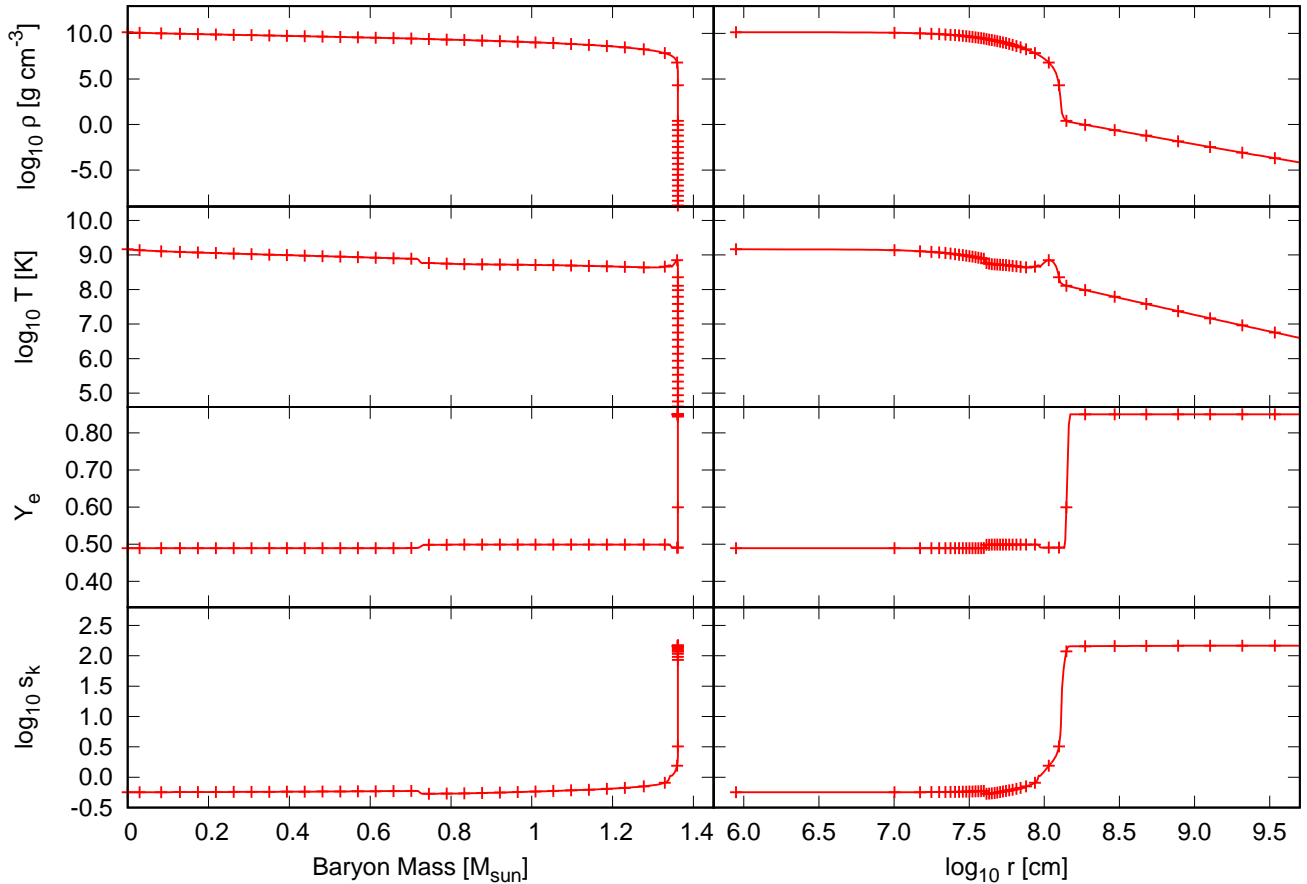


Figure 1. Distributions of density (top), temperature (second top), electron mole fraction (third top), and entropy per baryon (bottom) of the initial model T9.0. As the horizontal axis, mass coordinate (left) or radius (right) are taken. Crosses indicate quantities every ten grids to show the resolution of the calculation.

the stability of the calculation. The mass of the core is increased with a constant rate of $1.0 \times 10^{-6} M_{\odot} \text{ yr}^{-1}$. The value is fairly consistent with recent estimates of a mass accretion rate of thermal-pulses in a SAGB star (Poelarends et al. 2008; Siess 2010). Note that although the rest time until collapse significantly depends on the mass accretion rate, the core structure does not much depend on the rate (Takahashi et al. 2013).

New rates for electron capture reactions by isotopes of ^{20}F , ^{20}Ne , ^{23}Na , ^{24}Na , ^{24}Mg , ^{25}Mg , and ^{27}Al calculated by Suzuki et al. (2016) are applied. Because the data table by Oda et al. (1994) is more sparse especially for the density grid, the steep rise in the electron capture rate around the critical density has not been well resolved. Accordingly, the reaction rates have been underestimated in our previous calculation. As a result of using the new rates, for example, electron capture by ^{24}Mg initiates when the central density reaches $4.5 \times 10^9 \text{ g cm}^{-3}$ in the current calculation, which is earlier than the previous result of $7.6 \times 10^9 \text{ g cm}^{-3}$. However, usage

of those new rates do not significantly alter the result, since both rates agree for much higher density than the critical density.

After the evolution calculation, an SAGB envelope having a physically consistent structure has been recovered on the highly degenerate ONe core. First, the surface structure of the ONe core is reconstructed by integrating four stellar equations (e.g., Kippenhahn & Weigert 1990). The integration starts from a point at which the entropy per baryon becomes $s_k = 2.0 \text{ kB}$. Note that time derivative terms of Tds/dt and dv/dt are set to be zero as we do not have information of the previous time step. Constant composition is taken from the point (mostly being composed of carbon and oxygen; $X(\text{C}) = 0.370$ and $X(\text{O}) = 0.581$) and is applied for the core surface layer during the integration. At a point where the boundary condition of $D \equiv 2U + V - 4 = 0$ (Sugimoto & Fujimoto 2000) is fulfilled, the luminosity and composition are artificially changed. A hydrogen rich composition is applied,

$X(\text{H}) = 0.70$ and $X(\text{He}) = 0.21$. The luminosity of the envelope is tuned so that a reasonable amount of mass ($\sim 1 M_{\odot}$) is enclosed inside a reasonable radius ($\sim 100 R_{\odot}$).

The initial structure has a steep gradient of density and temperature at the boundary between the core and the envelope. In order to resolve the steep gradient, we apply an improved grid reconstruction method, which is described in the Appendix.

3.2. Model N8.8: Nomoto's progenitor

The other progenitor model we use is a $2.2 M_{\odot}$ He star model calculated by Nomoto (1984, 1987)². We refer to this model as the model N8.8 hereafter. This progenitor has formed a cool $1.3769 M_{\odot}$ ONe core. Prior to collapse, electron mole fraction of the central $\sim 0.7 M_{\odot}$ region is slightly reduced to 0.488, while outer region in the core has a uniform Y_e of 0.50. The central $\sim 0.1 M_{\odot}$ region has already experienced a passage of the ONe deflagration and has a small electron mole fraction and high temperature and entropy. The ONe core is surrounded by a diffuse hydrogen-rich envelope, which has been attached from a point where the density is $3.54 \times 10^3 \text{ g cm}^{-3}$. The envelope extends to $1.09 \times 10^9 \text{ cm}$ and has Y_e of 0.60.

The new grid reconstruction method is also applied for this progenitor to yield well defined grid points for the hydrodynamic calculation. The result is shown by Fig. 2. Due to the remapping process the core mass of this initial condition is slightly reduced from the original value of $1.3769 M_{\odot}$ to $1.3703 M_{\odot}$. The initial condition is not in a hydrostatic equilibrium, probably due to the low Y_e at its center.

4. RESULT OF THE MODEL T9.0

Hydrodynamic evolution of the model T9.0 is calculated for 0.3942 s. Core bounce takes place 0.2830 sec after the calculation starts. Hence hereafter we use the post bounce time, $t_{\text{pb}} = (\text{calculation time}) - 0.2830 \text{ s}$, for a time indicator in addition to the calculation time. Trajectories as well as the evolution of the flame and the shock fronts are shown in Fig.3 using the post bounce time.

4.1. Until core bounce

4.1.1. Oxygen+neon ignition

At 0.1507 sec after the calculation begins ($t_{\text{pb}} = -0.1323 \text{ s}$), oxygen and neon at the center of the star

is burned out. Because of the high electron degeneracy, oxygen+neon burning in the ONe core becomes a runaway reaction. The nuclear reaction increases the temperature but the degenerate pressure only slightly rises at the same time. The rise of the temperature significantly enhances the reaction rate, and the rate of the temperature rise is recursively enhanced. As a result, the reaction proceeds much faster than the hydrodynamical response time. Because of the high temperature, the reaction finally reaches a reaction equilibrium as a steady state, and NSE is established for the chemical composition.

Three causes can contribute to the central temperature increase in the ONe core to trigger the runaway nuclear burning. The first one is adiabatic compression, the second is electron capture reactions onto ^{20}Ne and ^{24}Mg , and the third is nuclear reactions of oxygen+neon burning itself. Until the nuclear burning significantly changes the chemical composition, a temperature rise can be separated into two terms:

$$\frac{\Delta T}{T} = \frac{\Delta T_{\text{comp}}}{T} + \frac{\Delta T_{\text{reac}}}{T} \quad (23)$$

$$\equiv \left(\frac{\partial \ln T}{\partial \ln \rho} \right)_{s_k} \frac{\Delta \rho}{\rho} + \left(\frac{\partial \ln T}{\partial \ln s_k} \right)_{\rho} \frac{\Delta s_k}{s_k}. \quad (24)$$

The density rise increases the temperature through the first term in the r.h.s., and the entropy change due to reactions affects through the second term. For the central grid, time evolution of these two terms until ignition are shown in Fig. 4. The assumption that the chemical composition only slightly changes during the temperature rise can be verified since the summation of the two terms, $\Delta T_{\text{sum}} \equiv \Delta T_{\text{comp}} + \Delta T_{\text{reac}}$, well explains the evolution of the total temperature difference. This figure shows that the central temperature steadily increases not by heating but by compression for the first $\sim 0.1 \text{ s}$. Then, after the temperature increases by $\sim 0.02 \text{ MeV}$, the runaway heating by the nuclear reaction initiates. The initial central temperature is 0.12 MeV. Therefore the heating by oxygen+neon burning is estimated to be dominant after the temperature rises to $\sim 0.14 \text{ MeV}$. The heating rate exceeds $\sim 1 \times 10^{16} \text{ erg g}^{-1} \text{ sec}^{-1}$ at this moment and keeps increasing.

Thus, the adiabatic compression importantly increases the central temperature of the model T9.0. This is because the initial structure of the model T9.0 is nearly but not completely in the hydrostatic equilibrium, so that the core slowly contracts from the start of the calculation. Despite the effort of remapping the structure as consistent as possible, the loss of the hydrostatic equilibrium is likely due to the remapping process from the stellar evolution calculation to the hydrody-

² This model has been often referred to as a “8.8 M_{\odot} ECSN progenitor” in the supernova community (Janka et al. 2008; Fischer et al. 2010; Radice et al. 2017).

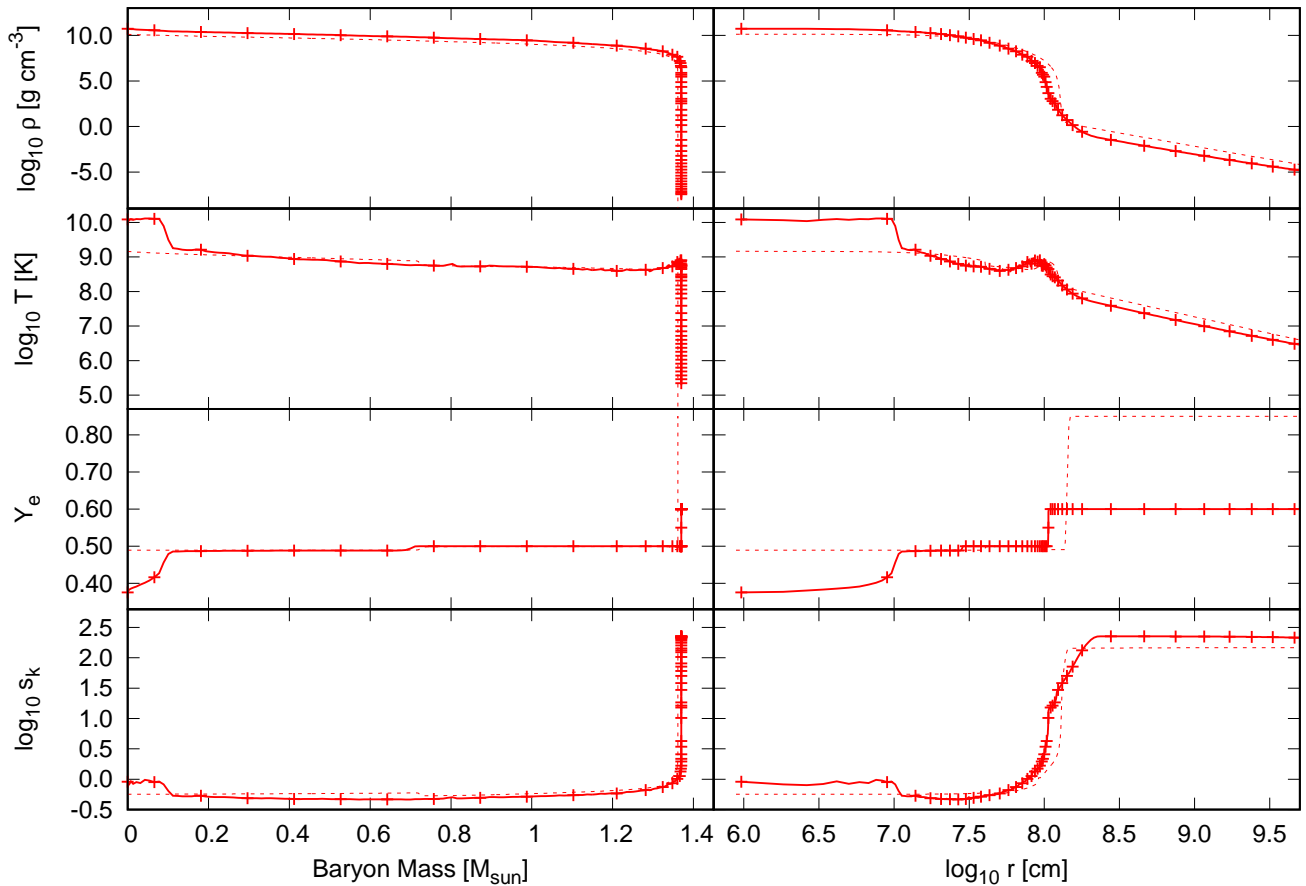


Figure 2. Same as Fig.1 but for model N8.8. Distribution of model T9.0 is overlaid as thin dashed lines for the sake of comparison.

dynamic calculation, because a much longer contraction timescale has been obtained in the evolution calculation. This suggests that the ONe core in reality can be hydrostatic even at the moment of the central ignition. In order to investigate how the different degree of the initial hydrostatic/dynamical stability affects the late core evolution, we have conducted a similar hydrodynamical calculation using an ONe core model in which the central Y_e distribution is artificially changed to ensure the initial hydrostatic stability. The result is reported in §4.3.

Our hydrodynamical calculation does not include heating by electron capture reactions onto ^{20}Ne and ^{24}Mg . However, this can be well justified because the progenitor structure just before the central ignition is taken from the evolution calculation for the initial condition. Here we give an estimate for the heating effect of the electron capture reaction by ^{20}Ne . The reaction accompanies the other electron capture by ^{20}F , and one sequential electron capture heats the surroundings by $2\mu_e + \mu_{^{20}\text{Ne}} - \mu_{^{20}\text{O}} - 2E_\nu$, where $2E_\nu$ shows

energy emitted by neutrinos, which are assumed to escape from the system at this stage. Stellar evolution calculation provides values of $\mu_e \sim 10$ MeV, $\mu_{^{20}\text{Ne}} - \mu_{^{20}\text{O}} \sim \Delta m_{^{20}\text{Ne}} c^2 - \Delta m_{^{20}\text{O}} c^2 = -10.8$ MeV, and $2E_\nu \sim 0.8 + 2.7$ MeV with the electron capture rate of $dY_{^{20}\text{Ne}}/dt \sim 9.0 \times 10^{-5} \text{ sec}^{-1} \text{ baryon}^{-1}$. The equivalent heating rate is $\sim 4.9 \times 10^{14} \text{ erg g}^{-1} \text{ sec}^{-1}$. Thus, an entropy change during a short period Δt becomes $\Delta s_k = (\epsilon_{ec} \Delta t)/T \sim 5.1 \times 10^{-4} \times (\Delta t/0.1\text{s}) \text{ baryon}^{-1}$ with the temperature of $T \sim 0.1$ MeV. As the initial entropy of the core is $s_k \sim 0.5$, this gives $\Delta T_{\text{heat}}/T \sim 3.2 \times 10^{-3}$ for $\Delta t = 0.1$ sec, which is much smaller than the effect of compression.

4.1.2. Flame propagation and neutrino radiation

As a result of the oxygen+neon burning, the NSE region has the entropy per baryon of $s_k \sim 1.5$ as well as the high temperature of $T \sim 1.1$ MeV ($\sim 1.3 \times 10^{10}$ K). The NSE region is surrounded by a still cold ($s_k \sim 0.5$ and $T \sim 0.1$ MeV $\sim 1.2 \times 10^9$ K) ONe region. In this simulation, the boundary layer that connects the hot ash and

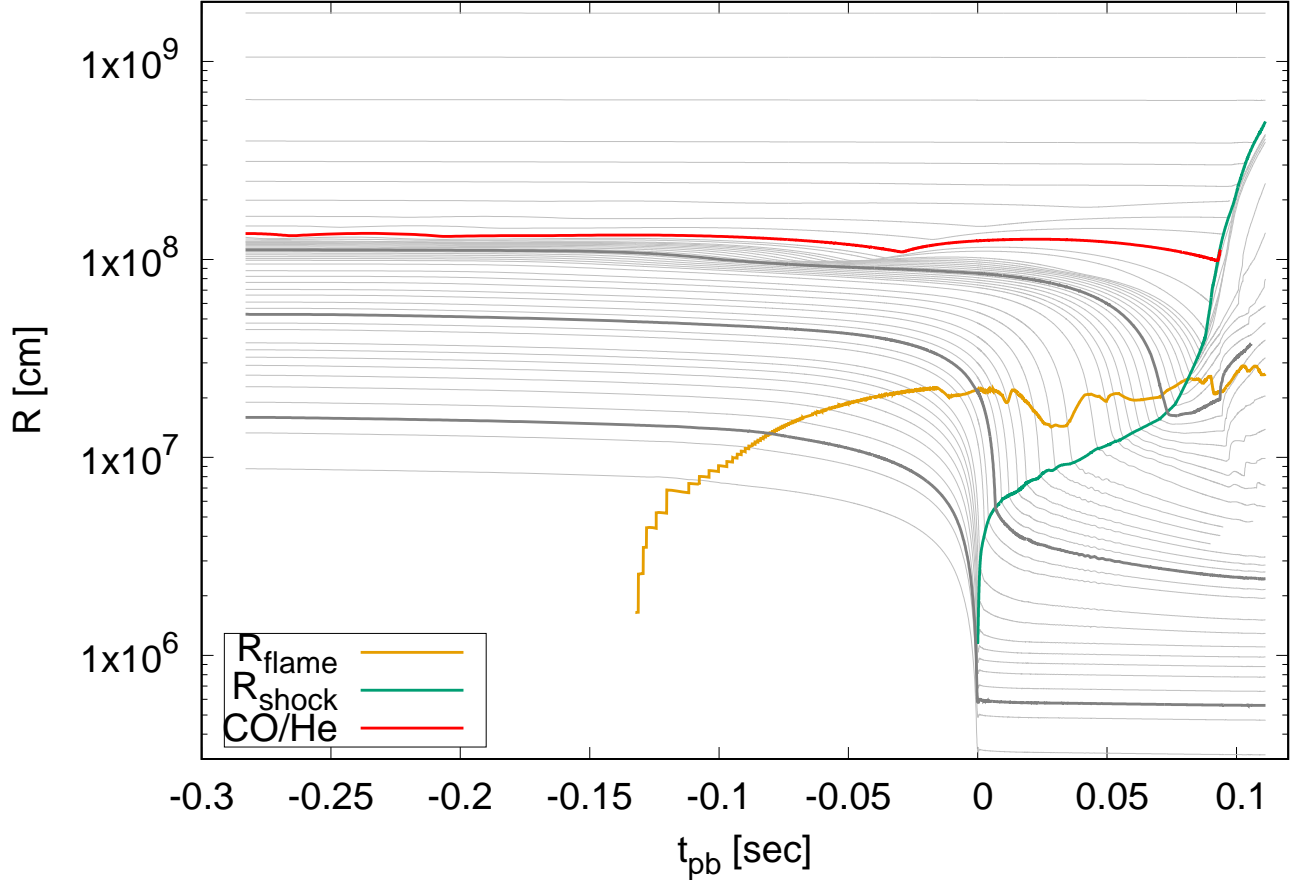


Figure 3. Trajectories of Lagrangian grids are shown for the model T9.0. Grids of 0.100 , 1.000 , and $1.360 M_{\odot}$ are shown by black thick lines, and the boundary between CO and He compositions ($1.36145 M_{\odot}$) are shown by the red thick line. Radii of the flame and shock fronts are shown by thick orange and thick green lines respectively.

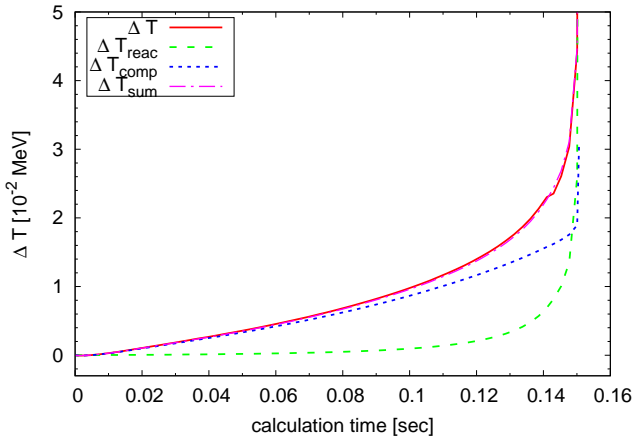


Figure 4. Details of the prior temperature rise at the center of the star, calculated for model T9.0. See the text for definitions of each temperature difference.

cold fuel is resolved by a one-dimensional zoning with a radial resolution of $\gtrsim 10^6$ cm. With this resolution,

the boundary layer looks like a discontinuity surface in terms of temperature and chemical composition, which is hereafter referred to as a flame front.

As time passes, the flame front moves outward and finally reaches $\sim 1.0 M_{\odot}$ by core bounce. The propagation speed of the flame front is shown in Fig.5. The propagation velocity in the observer frame, V_{obs} , is calculated as the time derivative of the radius of the flame front, r_f . To do so, the original saw-tooth-shape data of r_f (shown by the dashed line in the top panel) is numerically smoothed to make a continuous data (solid line). The contraction speed at the flame front, V_{cont} , is calculated every 0.01 sec before the core bounce. Finally, the flame propagation velocity in the comoving frame, or the local propagation velocity V_{prop} , is calculated as $V_{\text{prop}} = V_{\text{obs}} - V_{\text{cont}}$.

Until $t_{\text{pb}} \sim -0.04$ sec, or until the flame front passes the inner $0.3 M_{\odot}$, V_{prop} roughly keeps a constant value of $\sim 2 \times 10^8$ cm sec $^{-1}$ except for the first ignition phase. Later, the local propagation velocity as well as the con-

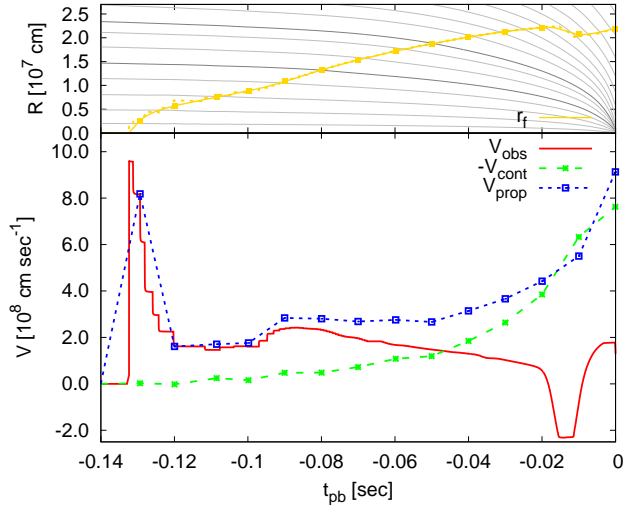


Figure 5. Time evolution of the radius of the flame front (top) and the propagation velocities (bottom). For the flame radius, the original data is shown by the dashed line, while the smoothed data is shown by the solid line. Gray lines are trajectories of arbitrarily selected Lagrangian grids (thin) or 0.1 and 0.3 M_{\odot} grids (thick). For the flame velocities, lines are the propagation velocity in the observer frame (red, solid), the contraction velocity at the flame radius (green, dashed), and the local propagation velocity (blue, dotted), respectively. The contraction velocity is calculated every 0.01 sec before the core bounce, which are indicated by points in the figure.

traction velocity are accelerated. V_{prop} reaches 9.1×10^8 cm sec^{-1} at core bounce, however, the local propagation velocity never exceeds the sound velocity of the core, $\sim 1 \times 10^9$ cm sec^{-1} . Thus a super-sonic mode of flame propagation (detonation) does not take place here. Note that a negative bump of V_{obs} can be seen at $t_{\text{pb}} \sim -0.017 - -0.016$ sec. This is because the flame front is locally trapped at $\sim 0.7 M_{\odot}$. There is a temperature discontinuity, which is made by a convection powered by ^{20}Ne electron capture during a previous evolutionary stage. Although the existence of this discontinuity itself is debatable (e.g., Schwab et al. 2015), the stagnation of the flame front will have a minor effect for core collapse, since the collapse has already begun at this moment.

Evolution of distributions of density, temperature, electron mole fraction, and entropy per baryon until core bounce is shown in Fig.6. Inside the NSE region, fast electron capture on free protons rapidly reduces Y_e . The characteristic timescale depends on the mass fraction of the free protons. In a region where the electron mole fraction is still larger than ~ 0.4 , typically a mass fraction of 10^{-2} to 10^{-3} exists as free protons. This gives the electron reduction timescale of 0.01–0.1 sec for a typical density of $\sim 1 \times 10^{10}$ g/cm^3 . The proton mass fraction

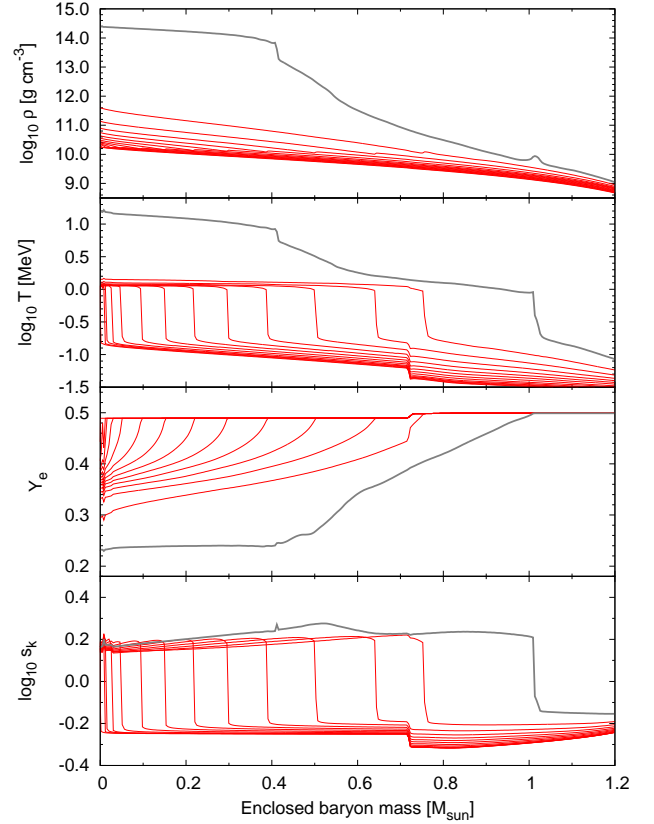


Figure 6. Evolution of distributions of density (top), temperature (second top), electron mole fraction (third top), and entropy per baryon (bottom) in the model T9.0 until core bounce takes place are shown. Thick gray lines are distributions at core bounce, while others are distributions every 0.01 sec before the core bounce.

decreases with decreasing Y_e . As a result, electron capture by heavy nuclei becomes important in a region with $Y_e \lesssim 0.36$. The electron capture reaction plays an important role for the core contraction. Firstly it reduces the degenerate pressure, by which the core is supported. Secondly, significant amount of energy is radiated away by neutrino emission when electron capture takes place.

In Fig.7, evolution of neutrino luminosities and mean neutrino energies recorded at the grid having the initial radius of 3×10^8 cm ($\sim c \times 0.01$ sec) are shown for three types of neutrinos of electron-type (red), anti-electron-type (green), and mu- and tau-neutrinos (blue). The ONe core starts to radiate ν_e just after the central ignition of oxygen and neon. The ν_e radiation is mainly due to the rapid electron capture by free protons and lasts for ~ 0.1 sec. Even before the core bounce takes place, the luminosity exceeds $L_{\nu_e} > 10^{51}$ erg sec^{-1} .

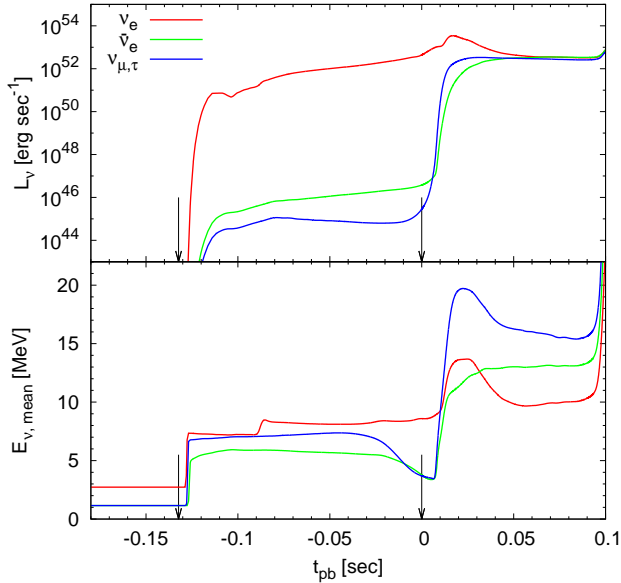


Figure 7. Time evolution of neutrino luminosities and mean neutrino energies for the model T9.0. Red, green, and blue lines correspond to electron type, anti-electron type, mu- and tau type neutrinos, respectively. Arrows indicate the time of ignition (left, at $t_{\text{pb}} = -0.1323$ sec) and of core bounce (right).

Similar to ν_e , other flavors of $\bar{\nu}_e$ and $\nu_{\mu,\tau}$ (as well as $\bar{\nu}_{\mu,\tau}$) are emitted from the central NSE region before the core bounce. In our simulation, these emissions are largely owing to thermal pair emissions of e^+e^- pair annihilation and plasmon decay, so that their luminosities of $L_\nu < 10^{46}$ erg sec $^{-1}$ are much smaller than that of ν_e . Recent works have revealed that β^+ decay of NSE isotopes enhances pre-core-bounce emission of $\bar{\nu}_e$ for both FeCC- and EC-SNe (Patton et al. 2017; Kato et al. 2017). The result for an ECSN in Kato et al. (2017), however, shows that the $\bar{\nu}_e$ luminosity resulting from the β^+ decay is only one order-of-magnitude larger than that of the thermal processes. Considering the far more energetic ν_e emission by the electron capture, the β^+ decay does not affect the pre-collapse hydrodynamic evolution of the ONe core.

Shortly after the core bounce, the neutrino burst takes place. The peak luminosities reach 3.5×10^{53} erg sec $^{-1}$ for electron-type neutrino and $\sim 3 \times 10^{52}$ erg sec $^{-1}$ for other types as well. The ν_e and $\bar{\nu}_e$ mainly originate from electron- and positron-capture reactions, and thermal processes of e^-e^+ -pair process and bremsstrahlung are responsible for ν_μ and ν_τ emissions. β^+ decays and positron captures on NSE isotopes might be important for $\bar{\nu}_e$ emission in the neutrino burst, though these have not been investigated in detail so far. Note that the in-

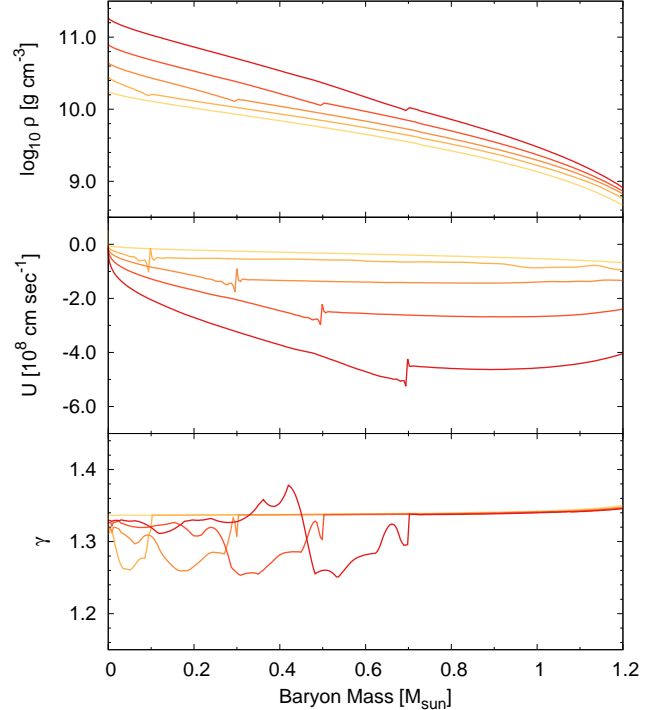


Figure 8. Evolution of distributions of the density (top), the velocity (middle), and the adiabatic index (bottom). Times are selected when the ignition takes place at the center ($t_{\text{pb}} = -0.1323$ s, light-yellow) and when the flame front reaches $0.1 M_\odot$ ($t_{\text{pb}} = -0.0793$ sec, light-orange), $0.3 M_\odot$ ($t_{\text{pb}} = -0.0496$ sec, orange), $0.5 M_\odot$ ($t_{\text{pb}} = -0.0302$ sec, dark-orange), and $0.7 M_\odot$ ($t_{\text{pb}} = -0.0164$ sec, red), respectively.

crease in luminosities and mean energies at $t_{\text{pb}} \sim 0.1$ sec is caused by sudden acceleration of the referenced grid up to the speed of light.

The intense radiation of electron-type neutrino before the core bounce will be a distinctive feature of the ONe core collapse compared with a Fe core collapse. The electron capture in a collapsing Fe core is driven by both free-protons and NSE isotopes and it lasts for ~ 100 sec until core bounce. Recently Kato et al. (2017) have analyzed the neutrino radiation during pre-bounce phases for collapsing ONe and Fe cores and estimated their detectability for present and future neutrino detectors. They have found that event numbers of ν_e from the ONe core collapse are expected to be more than one order of magnitude larger than Fe core collapse, while the number of $\bar{\nu}_e$ events of ONe core collapse is much less, if they take place at the same distance of 200 pc from the earth. This work provides the theoretical understanding of differences between the two cores.

The other important consequence of the phase transition is that the adiabatic index γ is significantly lowered

when the region becomes NSE. In Fig.8, evolution of distributions of the density (top), the velocity (middle), and the adiabatic index (bottom) are shown. Times are selected when the ignition takes place at the center and when the flame front reaches 0.1, 0.3, 0.5, and 0.7 M_{\odot} . This figure clearly shows that the hydrodynamical instability due to the photo-disintegration, which is known to trigger the core collapse of a Fe core, also develops in the ONe core. Core contraction is accelerated by this instability, and runaway collapse takes place in the end.

4.1.3. Effect of neutrino-electron scattering to the flame propagation

The flame front propagates as the temperature of the flame-above region firstly increases and successively a runaway nuclear reaction sets in combusting the fuel into the ash. Because of the runaway nature of the nuclear reaction, the overall timescale of the flame propagation is mainly determined by the timescale of the mechanism that is responsible for the prior temperature rise.

Heat conduction at the flame front has been considered as a main driving mechanism of the laminar flame in an ONe core. Applying eq.(44) in Timmes & Woosley (1992), the laminar flame driven by heat conduction in our calculation is estimated to have a slow velocity of $\lesssim 7 \times 10^6$ cm s⁻¹ until $t_{\text{pb}} \sim -0.05$ sec because of the small oxygen mass fraction of $X(\text{O}) \sim 0.48$. This is more than one-order-of-magnitude less than the local flame propagation velocity of $V_{\text{prop}} \sim 10^8$ cm sec⁻¹ obtained in this work. This will not only give a justification of omitting heat conduction from our calculation, but also indicate the existence of other driving mechanisms of the flame front propagation in the ONe core. Note that the propagation velocity of the conductive flame can be enhanced due to the burning front corrugation, therefore the above estimate actually gives the lower limit of the propagation velocity of the conductive flame. We will briefly discuss this effect later in §6.2.

In order to find what kind of mechanisms are operating in this simulation, the detail of the local temperature rise is analyzed as shown in Fig.9. Differences between the initial values and the values when the local temperature exceeds a critical temperature of 0.16 MeV are used to calculate ΔT , ΔT_{comp} , and ΔT_{reac} in this figure. Hereafter we refer to the temperature rise up to the 0.16 MeV as the prior temperature rise, since the nuclear heating rate exceeds $\sim 3 \times 10^{17}$ erg g⁻¹ s⁻¹ at this point and a time to reach NSE becomes less than $\sim 10^{-3}$ sec after that. This figure shows that the adiabatic compression is the main effect for the prior temperature rise for the inner $\sim 0.7 M_{\odot}$ region. In this meaning, this flame propagation is not a pure deflagration, in which the flame front propagation is predominantly powered

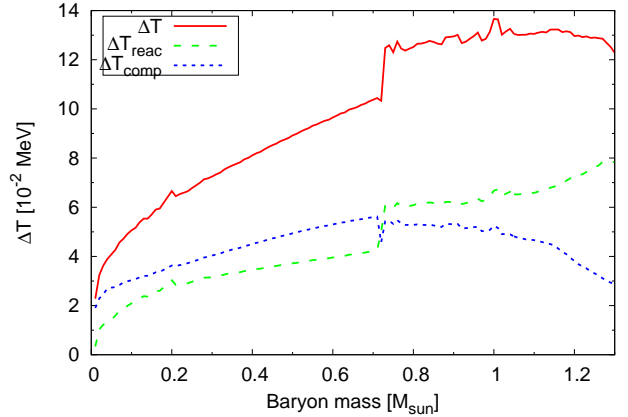


Figure 9. The distribution of the prior temperature rise for the model T9.0. See text for definitions of ΔT s.

by a certain mechanism of heat transfer. Meanwhile, not only compression but also heating by reactions plays an important role in our simulation as well, especially for the outer region of $\gtrsim 0.2 M_{\odot}$. The heating term even overcomes the other for the outer region of $> 1.00 M_{\odot}$.

We have found that neutrino-electron scattering is the most contributing reaction for the prior heating. Because of the fast electron capture reactions, the inner NSE region radiates high energy electron-type neutrinos with a considerable luminosity (Fig.7). A part of these neutrinos hit the surroundings providing energy to heat up the material. Distributions of heating rates and the energy flux of the electron type neutrino taken at $t_{\text{pb}} = -0.08$ and -0.04 sec are shown in Fig.10. The heating rate by oxygen+neon burning shown as ϵ_{nuc} has a sharp peak in front of the flame front and a steep decline in the outer region. On the other hand, the electron scattering shown as ϵ_{esc} widely heats the flame-above region with a heating rate of $\sim 3 \times 10^{17}$ erg g⁻¹ sec⁻¹. Hence, the local temperature of the flame-above region increases due to the combination of the compression and the neutrino-electron scattering. The prior temperature rise leads to the runaway nuclear burning when the local temperature exceeds 0.16 MeV, with which the nuclear heating rate corresponds to $\sim 3 \times 10^{17}$ erg g⁻¹ sec⁻¹.

One may have suspicions about the high efficiency of the neutrino-electron scattering. Indeed, the reaction has a small cross section of $\sigma_{\text{esc}} \sim 0.06 \times \sigma_0 (\frac{E_{\nu}}{m_e c^2})^2 (\frac{E_{\nu}}{\mu_e})$, where E_{ν} is the scattered neutrino energy and $\sigma_0 \equiv \frac{4}{\pi} (\frac{m_e c^2}{h})^4 (\frac{G_F}{m_e c})^2 = 1.76 \times 10^{-44}$ cm² (Shapiro & Teukolsky 1986). The mean neutrino energy during this phase is $E_{\nu} \sim \mu_e \sim 8$ MeV (see Fig.7). Thus the cross section becomes $\sigma_{\text{esc}} \sim 2.7 \times 10^{-43}$ cm², and the corresponding neutrino mean free path is $l_{\text{esc}} = 1/n_e \sigma_{\text{esc}} \sim 1.23 \times 10^9$ cm for $\rho Y_e = 0.5 \times 10^{10}$ g

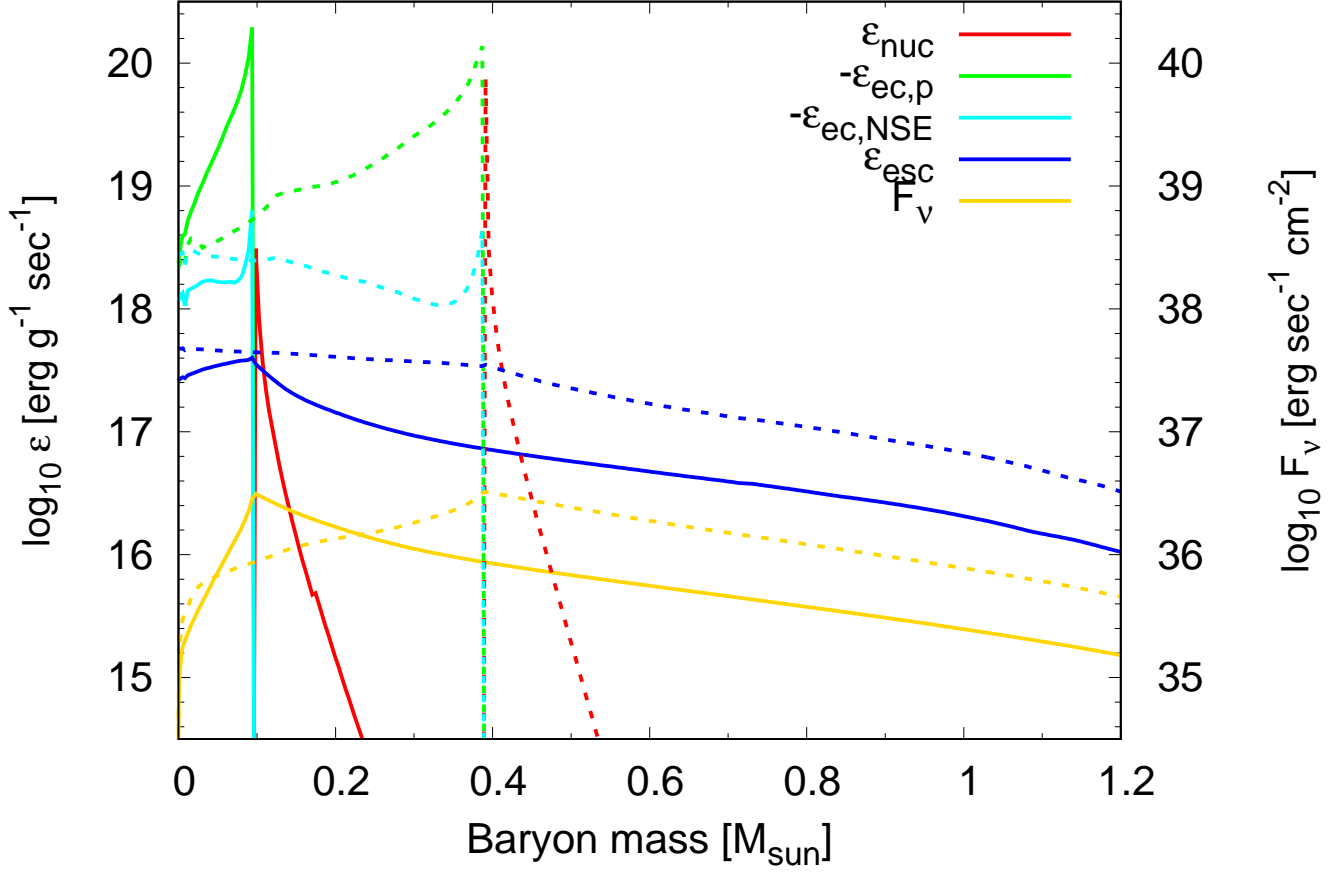


Figure 10. Distributions of heating rates and the energy flux of the electron type neutrino are shown. Results taken at $t_{pb} = -0.08$ sec are shown by solid lines, while results at $t_{pb} = -0.04$ sec are by dashed lines. Heating rates of the nuclear burning (ϵ_{nuc}), the electron capture by free protons ($-\epsilon_{\text{ec,p}}$) and by NSE isotopes other than proton ($-\epsilon_{\text{ec,NSE}}$), and the neutrino-electron scattering (ϵ_{esc}) are shown by red, green, light-blue, and blue lines, respectively. Note that electron capture reactions actually cools the NSE region, so that the original $\epsilon_{\text{ec,S}}$ are negative. The energy flux of the electron type neutrino is shown by yellow lines.

cm^{-3} . This is 100 times larger than the radius of the flame propagation region of $\sim 10^7$ cm.

None the less, the heating rate of $\sim 3 \times 10^{17}$ erg g^{-1} sec^{-1} can be estimated as follows. First, the neutrino energy flux F_ν at the flame front of the radius r_f is estimated as

$$4\pi r_f^2 F_\nu = 4\pi r_f^2 E_\nu D_{\text{ec}} \lambda_{\text{ec}}, \quad (25)$$

where D_{ec} is a thickness of an electron capture region and λ_{ec} is the electron capture rate per unit volume. Since the electron capture is rapid, the thickness can be estimated as $D_{\text{ec}} = V_f \tau_{\text{ec}}$ with the flame propagation velocity V_f and the timescale of the electron capture τ_{ec} . As $\lambda_{\text{ec}} = \rho Y_e / m_u \tau_{\text{ec}}$, this yields

$$\frac{F_\nu}{E_\nu} = V_f \frac{\rho Y_e}{m_u}. \quad (26)$$

Suppose that 50% of the energy of the neutrino is passed to the electron by this scatter, an energy deposit rate of a neutrino that travels a short length Δr relates to the energy flux as

$$4\pi r_f^2 \Delta r \rho \epsilon_\nu = 0.5 \times 4\pi r_f^2 F_\nu \times \Delta r / l_{\text{sc}}, \quad (27)$$

and the rate reduces to

$$\epsilon_\nu = 0.5 \times V_f E_\nu \left(\frac{Y_e}{m_u} \right)^2 \rho \sigma_{\text{esc}} \quad (28)$$

at the flame front. Providing $V_f = 2 \times 10^8$ cm sec^{-1} , $E_\nu = 8$ MeV, $Y_e = 0.5$, and $\rho = 1 \times 10^{10}$ g cm^{-3} , it gives $\epsilon_\nu \sim 3.13 \times 10^{17}$ erg g^{-1} sec^{-1} and well explains the simulation result. The radius dependence may be obtained by multiplying a factor of $(r/r_f)^{-2}$.

In order to confirm the importance of the contribution of the neutrino-electron scattering, another hydro-

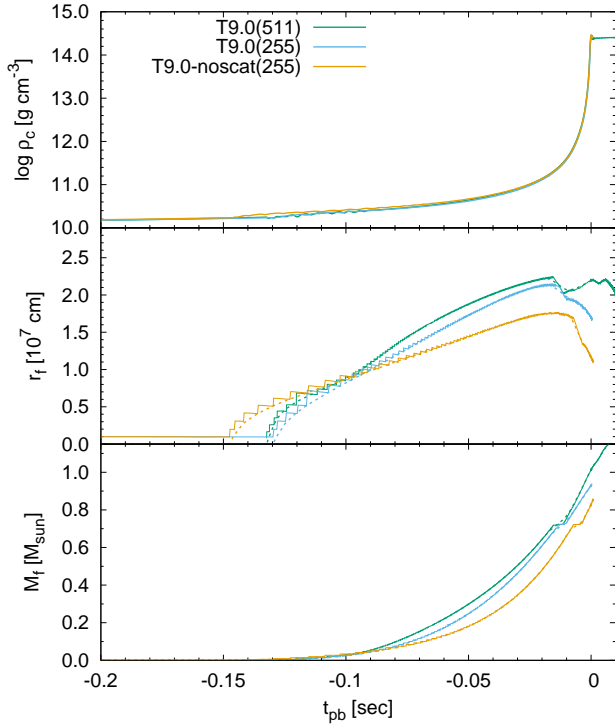


Figure 11. The time evolution of the central densities (top), the radii of the flame fronts (middle), and the mass coordinates of the flame front (bottom) are shown for the model T9.0. The original result obtained with 511 grids is shown by green lines, while the result with 255 grids are by cyan lines. The result of the model without neutrino-electron scattering is shown by orange lines.

dynamical calculation until core bounce is conducted using the model T9.0 deactivating the neutrino-electron scattering in the surrounding ONe region. The radial resolution is reduced to 255 grid points in this additional calculation. The reduction effect is minimized as the outermost grid is set to be at 3×10^8 cm, and we have confirmed that this resolution is enough to reproduce very similar flame propagation speed for the case with the neutrino-electron scattering. As expected, the adiabatic compression now explains vast majority of the prior temperature rise. The time until core bounce from the central ignition increases from the original 0.1322 sec to 0.1463 sec, and furthermore, the extension rates in terms of both the radius and the enclosed mass of the flame front are reduced in the case without the neutrino-electron scattering (Fig.11).

The potential importance of neutrino-electron scattering has been discussed by Chechetkin et al. (1976, 1980) for a degenerate CO core. In this work, we show that this mechanism actually effectively works in a highly degenerate ONe core, in which higher efficiency than in a

CO core is achieved by the higher density and the higher neutrino energy and luminosity. Note that electron capture on ^{20}Ne only partly accounts for the prior heating, because the heating rate is far below 3×10^{17} erg g^{-1} sec^{-1} . Heat conduction will be negligible as it results in a much slower propagation velocity discussed above. Also contributions of other neutrino reactions are estimated to be minor. This is discussed in §6.1.

There is a formal similarity between the heat conduction by relativistic degenerate electrons and the neutrino-electron scattering found in this simulation. In the former case, a high energy electron in a high temperature region hits matter in a low temperature region after traveling a mean free path of l_{cond} , transporting the energy. Similarly, in the latter case, a high energy neutrino created in the hot ash region hits an electron in a cold fuel region after traveling a mean free path of l_{sc} . In contrast, their length scales of the mean free paths are completely different. Because of the short length scale of $l_{\text{cond}} \sim 10^{-8}$ cm, the energy transfer by the relativistic degenerate electron takes place with large number of collisions between the electron and the matter, which can be well approximated as a diffusion process. On the other hand, a neutrino traveling through the ONe core interacts with electrons at most one time, because $l_{\text{scat}} \sim 10^9$ cm is much larger than the radius of the flame propagation region. In this meaning, our simulation with a radial resolution of $\gtrsim 10^6$ cm well resolves the temperature structure developed by the neutrino-electron scattering.

4.2. After core bounce

Here we give a short summary of the later result from the core bounce until the shock front passes the original core surface of $\sim 10^8$ cm at $t_{\text{pb}} \lesssim 0.1$ sec. Although it is desired to conduct a longer simulation up to $t_{\text{pb}} \sim 1$ sec to determine the explosion properties such as the explosion energy and the remnant mass (c.f. Janka et al. 2008), our code has encountered a serious resolution problem after $t_{\text{pb}} \gtrsim 0.1$ sec, in which the post shock material is significantly heated by the shock heating due to coarse radial resolution in that region. This is why we have decided to focus on the early collapse phase of a highly degenerate ONe core in this work. Detail results and discussions for the explosion properties will be reported in the near future.

Core bounce leaves a nascent NS at the center of the star (we refer to the inner high density region with

³ The conductive mean free path is estimated using the opacity κ and the specific heat at constant pressure C_P as $l_{\text{cond}} \sim 4aT^3 / \rho^2 C_P \kappa$.

$\rho > 10^{11} \text{ g cm}^{-1}$ as the nascent NS hereafter). The nascent NS initially has a baryon mass of $0.4 M_{\odot}$ and successively grows by continuous mass accretion. A strong bounce shock develops from the surface and propagates outward. The propagation speed is initially fast and the shock passes through the inner $\sim 1.0 M_{\odot}$ region within 0.007 s. Then it decelerates, passing the next $\sim 0.36 M_{\odot}$ with 0.063 s. The newly born proto-NS radiates a significant amount of energy by neutrino radiation. The strong neutrino irradiation heats the accreting matter, keeping the flame front at a radius of $\sim 2 \times 10^7 \text{ cm}$ (see Fig. 3).

Mass accretion gradually ceases around $t_{\text{pb}} = 0.1 \text{ sec}$. With the decreasing ram pressure of the accretion flow, the shock rapidly accelerates to nearly the speed of light. At $t_{\text{pb}} = 0.1 \text{ sec}$, the shock completely passes through the core. At this moment, material of $\sim 0.02 M_{\odot}$ exists between the shock front and the surface of the nascent NS, and part of this is already unbound as enough energy has been provided by shock heating and neutrino reactions. The growing explosion energy, which is calculated as a sum of the thermal, kinetic, Newtonian gravitational, and nuclear binding energies of the unbound material, has already exceeded $\sim 4 \times 10^{49} \text{ erg}$ and is already larger than the binding energy of the envelope of this progenitor model of $\sim -1.4 \times 10^{49} \text{ erg}$. Thus, our calculation confirms the successful explosion from the highly degenerate ONe core progenitor.

4.3. Core collapse of a Y_e modified progenitor

The adiabatic compression plays an important role for triggering oxygen+neon burning in the model T9.0 even for the central ignition. This is because this initial condition is not in a complete hydrostatic equilibrium. The effect of the adiabatic compression will be minimized if the initial condition is hydrodynamically stable. In order to investigate how core collapse can be modified in this case, a Y_e modified progenitor model is additionally set and the core collapse is calculated until core bounce takes place.

This model is referred to as model T9.0ye in this work. Based on the model T9.0, the inner Y_e distribution is artificially increased from its original value 0.489 to 0.492. The model T9.0ye has an almost exact hydrostatic equilibrium: the structure is maintained more than 10^3 sec under a calculation without reactions. When the nuclear reaction is switched on, the high initial central temperature of $1.60 \times 10^9 \text{ K}$ allows oxygen and neon to burn within $7.4 \times 10^{-2} \text{ sec}$ from the initiation of the calculation. The ignition density becomes $1.63 \times 10^{10} \text{ g cm}^{-3}$. Core bounce takes place 0.3758 sec after the initiation of the calculation. Hence the model has a longer pre-

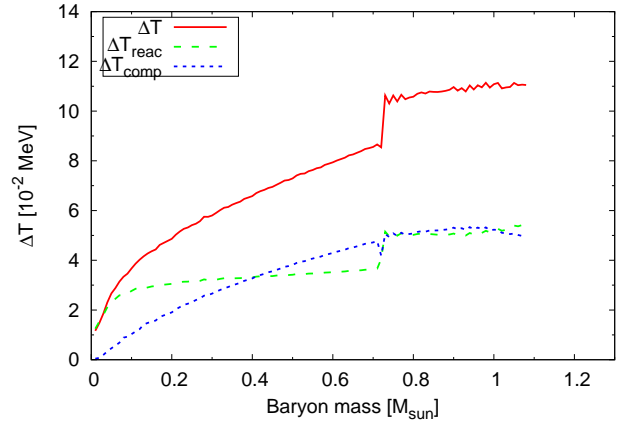


Figure 12. Same as Fig. 9 but for the model T9.0ye.

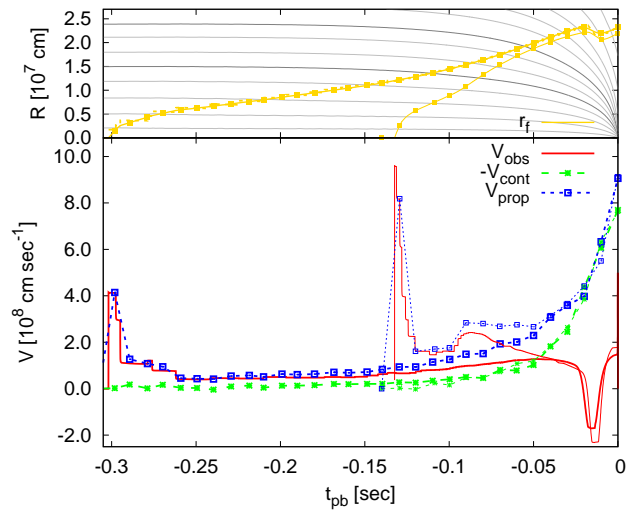


Figure 13. Same as Fig. 5 but for the model T9.0ye. Results of the model T9.0 are also shown by dashed lines.

bounce neutrino radiation phase of $\sim 0.30 \text{ sec}$ than the model T9.0.

Details of the prior temperature rise is shown in Fig.12. The temperature rise for the inner $\lesssim 0.2 M_{\odot}$ is largely explained by the neutrino heating. Contribution from the adiabatic compression is only minor. This means that, even though the adiabatic compression is almost absent, the neutrino heating alone can drive the flame propagation in this earlier phase. On the other hand, both the adiabatic compression and heating by the neutrino scattering cause the temperature rise for the outer region of $\gtrsim 0.3 M_{\odot}$ similar to the model T9.0.

The evolution of the propagation velocity is shown in Fig.13. Because of the smaller compression rate, the early flame propagation takes place much slower than in the model T9.0 and it takes about three times longer to propagate the inner $0.3 M_{\odot}$. Because the neutrino heat-

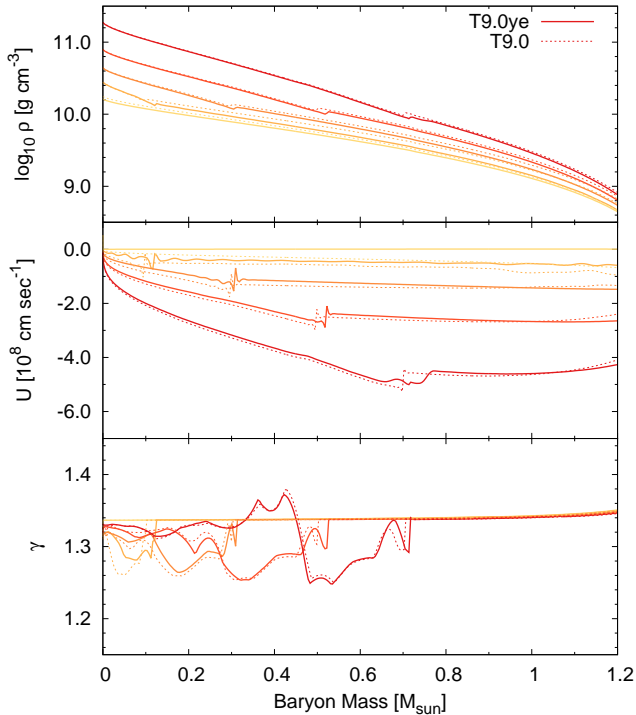


Figure 14. Same as Fig.8, but for the model T9.0ye. Results of the model T9.0 are also shown by dashed lines. Times are selected at the central ignition ($t_{pb} = -0.3018$ sec, light-yellow) and at when the flame front reaches $0.1 M_{\odot}$ ($t_{pb} = -0.0975$ sec, light-orange), $0.3 M_{\odot}$ ($t_{pb} = -0.0541$ sec, orange), $0.5 M_{\odot}$ ($t_{pb} = -0.0314$ sec, dark-orange), and $0.7 M_{\odot}$ ($t_{pb} = -0.0164$ sec, red), respectively.

ing rate depends on the propagation velocity (eq.28), the slow velocity lowers the neutrino heating rate. For instance, $\epsilon_{\nu} \sim 1.3 \times 10^{17}$ erg g^{-1} sec^{-1} when the flame front reaches $0.1 M_{\odot}$. After the front passes $\sim 0.3 M_{\odot}$, the core becomes unstable and starts to collapse. In the collapsing core, the adiabatic compression effectively causes the prior temperature rise, accelerating the flame propagation.

Finally, evolution of distributions of the density (top), the velocity (middle), and the adiabatic index (bottom) of models T9.0 and T9.0ye are compared in Fig.14. This figure clearly shows the similar dynamical evolutions of the two progenitors. A small difference in the velocity of $\sim 4 \times 10^7$ cm sec^{-1} can be seen for the initial distributions, which results from the different degree of the initial hydrostatic/dynamical stability. However, the two velocity distributions evolve almost identically through the collapse, since the contraction velocities are significantly accelerated.

5. RESULT OF THE MODEL N8.8

We calculate the evolution of the model N8.8 for 0.1310 sec in total. Trajectories of this model are shown in Fig. 15. The initial condition has a central NSE region of $\sim 0.1 M_{\odot}$ and the flame front is already located at 1.02×10^7 cm. Core bounce takes place after 5.07×10^{-2} sec from the start of the calculation. A successful explosion also takes place for this model in our work. Since we are focusing on the physics during the ONe core collapse, we leave detail analysis of the explosion for the future work. Here the result until core bounce is mainly discussed.

In Fig. 16, time evolution of the central density (top), the radius of the flame front (middle), and the mass coordinate of the flame front (bottom) are compared for the three initial models of T9.0 (green), T9.0ye (blue), and N8.8 (yellow). Most of the time, the flame front in the model N8.8 locates more inside than in the other two models in terms of both the radius and the mass coordinate. This more compact central NSE region originates from the initial structure. First of all, the initial model N8.8 is more compact than the model T9.0 in which the central density has already increased to 5.6×10^{10} g cm^{-3} , though the flame front still locates at $\sim 0.1 M_{\odot}$. This two times larger density having the same front position indicates that the early flame propagation velocity in the work by Nomoto (1987) might be much slower than in our model.

In Fig.17, the evolution of the neutrino luminosities and mean energies of the model N8.8 is compared with the results of the model T9.0. In spite of the more compact central NSE region, the results of the model N8.8 agree well with that of $t_{pb} > -0.05$ sec of the model T9.0. Having the smaller front radius with a comparable neutrino luminosity, the neutrino flux at the flame front in the model N8.8 becomes about two times higher than in the model T9.0. Distributions of heating rates and the energy flux of the electron type neutrino are compared in Fig. 18 for the two models. The about two times higher heating rate of neutrino-electron scattering in the model N8.8 results from the two times higher neutrino flux. Because of the higher heating efficiency, the neutrino scattering dominates the prior temperature rise in the model N8.8 (Fig. 19). Therefore, a more compact initial structure of the model N8.8 results in heating-dominated propagation of the flame front, which is qualitatively different from a propagation mechanism observed in the model T9.0.

However, in spite of the difference in the mechanism of the front propagation, the evolution of the central densities of the three models shown in Fig. 16 show striking resemblance for $t_{pb} > -0.05$ sec. In Fig. 20, the evolution of distributions of density, velocity, and adiabatic

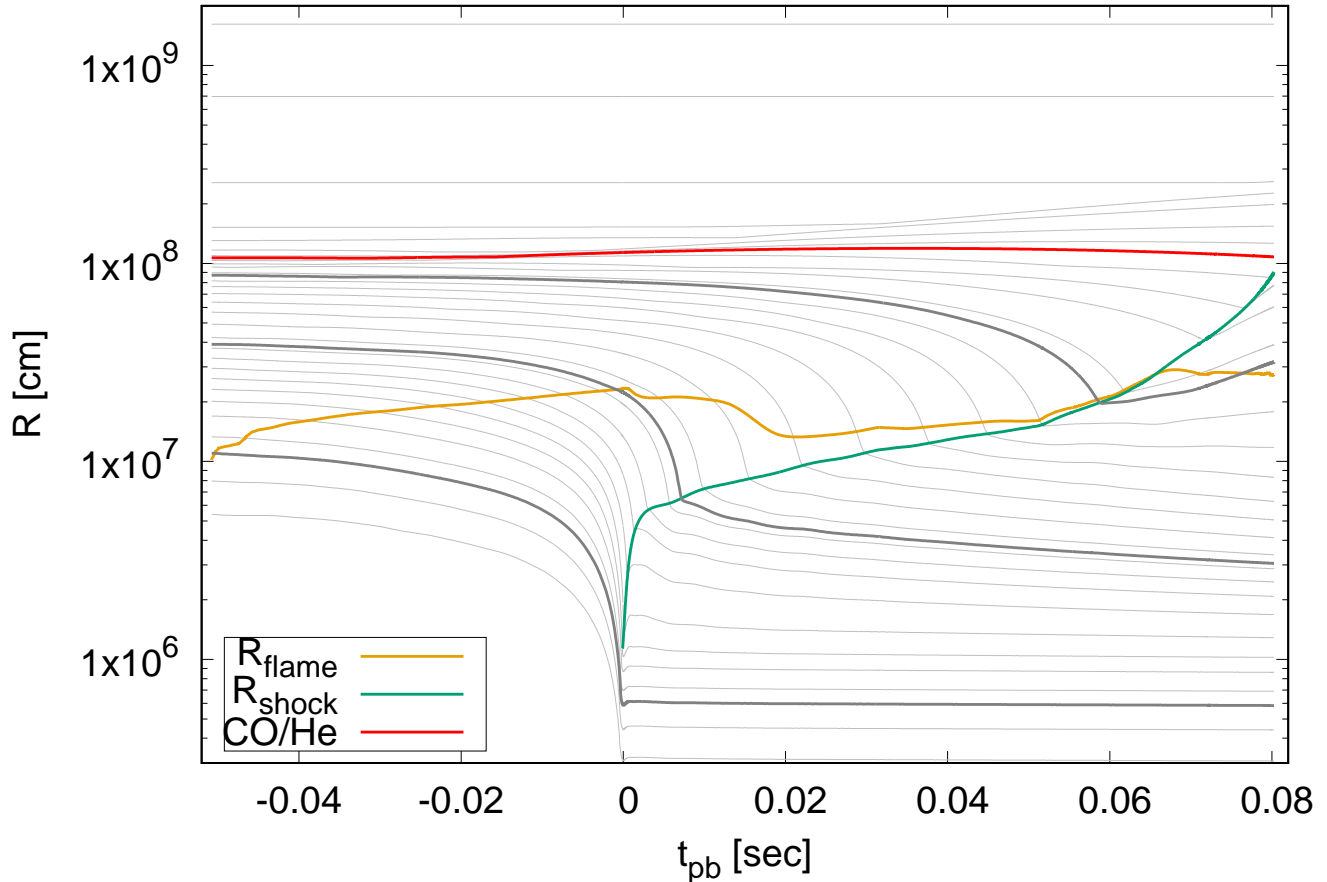


Figure 15. Same as Fig.3, but for the model N8.8. The enclosed baryon mass of CO/He boundary is $1.3703 M_{\odot}$.

index are compared for models of N8.8 and T9.0. The figure shows that the velocity evolution of the inner core coincides with each other, even though the model N8.8 develops oscillation in the outer region. This result indicates that there is a particular dynamical evolution of core collapse for the critical mass ONe core, which perhaps only slightly depends on how the deflagration propagates.

6. DISCUSSION

6.1. Prior heating by other neutrino reactions

We have shown that the neutrino-electron scattering effectively heats the surroundings to drive the flame front propagation in the ONe core. Here we estimate whether other neutrino heating mechanisms contribute to the prior temperature rise.

The first important result is that the neutrino emitted during the collapsing phase is dominated by the electron-type neutrino. This is because the electron-type neutrino is emitted by the electron capture reactions, while other types of neutrinos are only weakly

emitted from the low temperature ONe core. Accordingly, neutrino reactions that requires other types of neutrino of anti-electron-type neutrino absorption by nuclei ($\bar{\nu}_e + A \rightarrow e^+ + A'$), or inverse processes of thermal neutrino emissions, such as bremsstrahlung, pair-annihilation, and plasmon decay, hardly take place in the surrounding ONe region. Thus, possible candidates will be electron-type neutrino absorption by free-neutrons ($\nu_e + n \rightarrow e^- + p$), electron-type neutrino absorption by nuclei ($\nu_e + A \rightarrow e^- + A'$), neutrino-nucleon scattering ($\nu_e + p/n \rightarrow \nu_e + p/n$), and inelastic neutrino-nuclei scattering ($\nu_e + A \rightarrow \nu'_e + A^*$). Among them, the only possible candidates are inelastic neutrino-nuclei scattering and neutrino absorption by nucleus, because almost no free-nucleons exist in the outer cold ONe region.

It has been known that coherent scattering of neutrinos on nuclei ($\nu_e + A \rightarrow \nu_e + A$), the effect of which is taken into account for the NSE region in our calculation, is the dominant neutrino interaction in a collapsing Fe core (e.g., Bruenn & Haxton 1991). How-

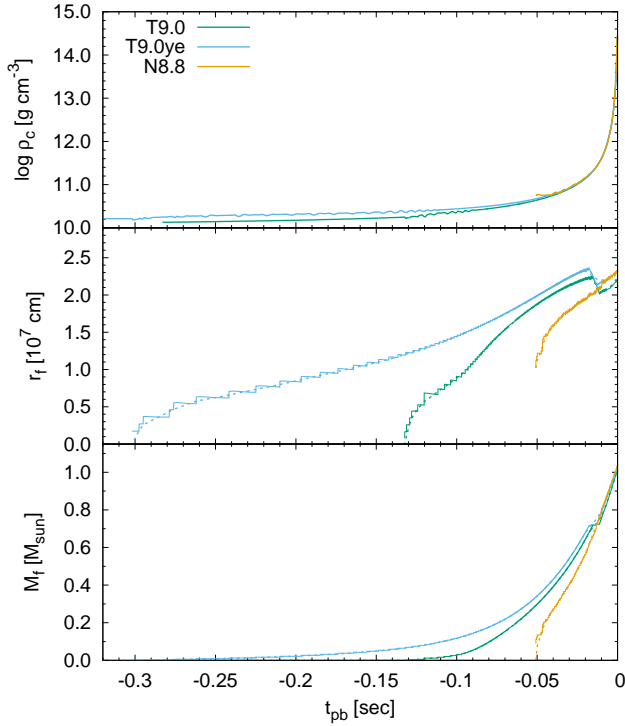


Figure 16. Same as Fig.11 but for models of T9.0, T9.0ye, and N8.8.

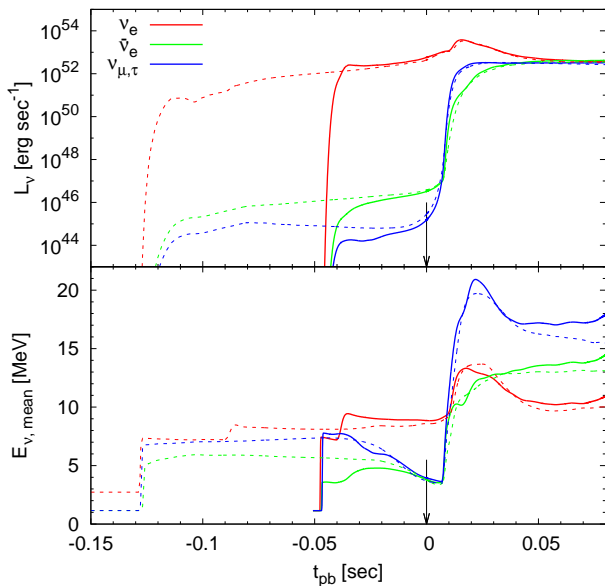


Figure 17. Same as Fig. 7 but for the model N8.8. Arrows indicate the time of core bounce. Results of the model T9.0 are also shown by dashed lines.

ever, this process does not contribute to matter heating, since rest mass of nuclei are much larger than the

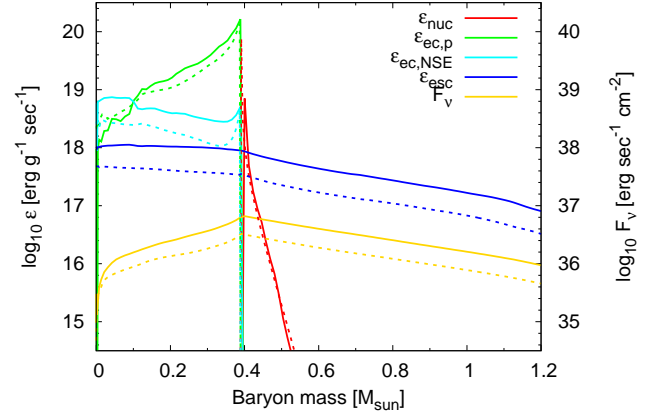


Figure 18. Same as Fig. 10 but for the model N8.8 at $t_{pb} = -0.03$ sec. Results of the model T9.0 at $t_{pb} = -0.04$ sec are also shown by thin lines.

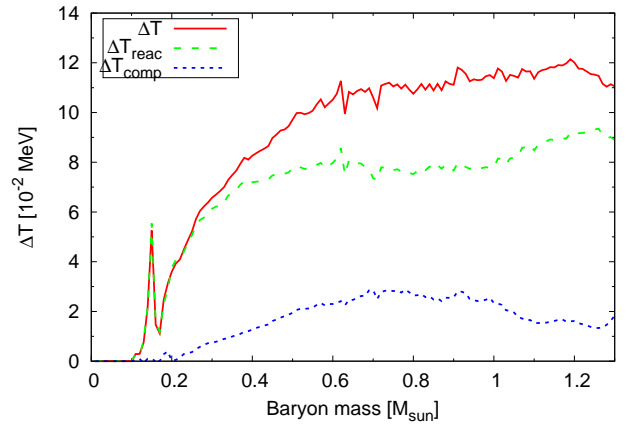


Figure 19. Same as Fig. 9 but for the model N8.8.

neutrino energy so that the scattering becomes almost elastic. Instead, inelastic neutrino-nuclei scattering is possible by exciting nuclei via neutral-current process, so that $\nu_e + A \rightarrow \nu'_e + A^*$. Bruenn & Haxton (1991) has shown that the cross section for ^{56}Fe can be as high as one-third of the neutrino-electron scattering cross section in a high temperature region of $T = 2 \times 10^{10}$ K. However, we expect that the heating effect in the ONe region will be minor. This is because, firstly, the ONe region is mainly composed of even-even nuclei, which requires a large neutrino energy for the excitation. This in turn suggests the small cross section of the reaction (Langanke et al. 2008). Furthermore, since the temperature of the ONe region is merely < 0.1 MeV, the effect of the thermal ensemble of the excited states (Sampaio et al. 2002; Juodagalvis et al. 2005; Dzhioev et al. 2011, 2014), which significantly en-

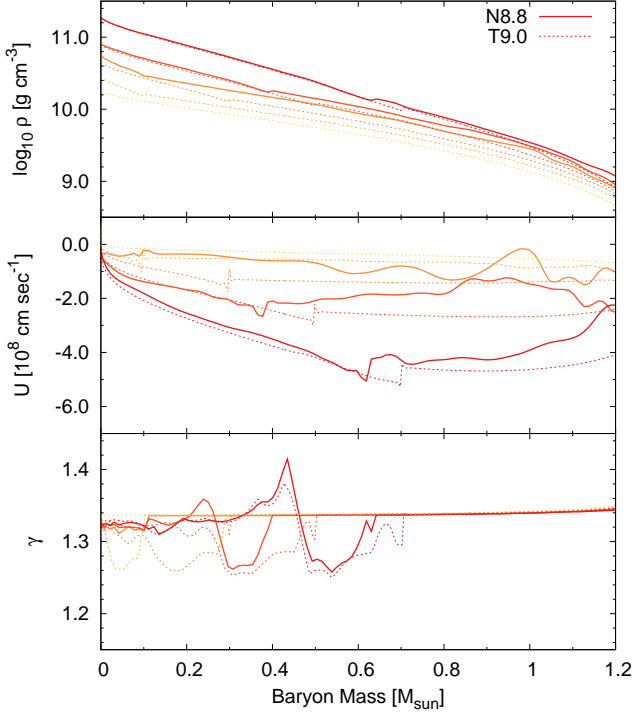


Figure 20. Same as Fig.8, but for the model N8.8. Results of the model T9.0 are also shown by dashed lines. Times are selected at when the central density reaches $5.64 \times 10^{10} \text{ g cm}^{-3}$ ($t_{\text{pb}} = -0.0503 \text{ sec}$, orange), $7.98 \times 10^{10} \text{ g cm}^{-3}$ ($t_{\text{pb}} = -0.0304 \text{ sec}$, dark-orange), and $1.89 \times 10^{11} \text{ g cm}^{-3}$ ($t_{\text{pb}} = -0.0164 \text{ sec}$, red), respectively.

hances the reaction rate especially for neutrinos with small energies of $\lesssim 10 \text{ MeV}$, will be negligible.

The heating rate of neutrino absorption by nuclei is estimated from the reaction rate of its inverse reaction of electron capture. Because of the detailed balance, the neutrino absorption kernel is related to the emission kernel as $R^a = \exp(\beta(E_\nu + \mu_{(A,Z)} - \mu_e - \mu_{(A,Z+1)}))R^e$. Similar to the discussion in section 2.2, the emission kernel is estimated as $R^e = ((hc)^3/4\pi c E_\nu^2)\lambda_{(A,Z+1)}\psi_{\nu,(A,Z+1)}n_{(A,Z+1)}$, where λ and ψ_ν are the reaction rate (s^{-1}) and the neutrino spectrum of the electron capture reaction by the $(A,Z+1)$ nucleus. Assuming that nuclei obey the Boltzmann statistic and $f_\nu \ll 1$, the collision term of the Boltzmann equation becomes

$$\begin{aligned} \left(e^{-\phi} \frac{\partial f_\nu}{c \partial t}\right)_{\text{coll}} &= R^e(1 - f_\nu) - R^a f_\nu \\ &\sim \frac{(hc)^3}{4\pi c E_\nu^2} \lambda_{(A,Z+1)} \psi_{\nu,(A,Z+1)} \\ &\times \left(n_{(A,Z+1)} - e^{\beta(E_\nu + \Delta_A - \mu_e)} n_{(A,Z)} f_\nu\right) \end{aligned} \quad (29)$$

where Δ_A is a mass difference between (A,Z) and $(A,Z+1)$ nuclei. The neutrino heating rate per unit mass can be equated with the rate of change of the specific neutrino energy density. Thus,

$$\begin{aligned} \rho_b \epsilon_\nu &= -e^{-\phi} \frac{\partial}{\partial t} \int \frac{d^3(p_\nu c)}{(hc)^3} E_\nu f_\nu \\ &\sim \int E_\nu \lambda_{(A,Z+1)} \psi_{\nu,(A,Z+1)} \\ &\times \left(e^{\beta(E_\nu + \Delta_A - \mu_e)} n_{(A,Z)} f_\nu - n_{(A,Z+1)}\right) dE_\nu \end{aligned} \quad (31)$$

is obtained. By approximating $\psi_{\nu,(A,Z+1)} \sim \delta(E_\nu - E_{(A,Z+1)})$ where $E_{(A,Z+1)}$ is a mean energy of neutrino emitted by the electron capture on the $(A,Z+1)$ nucleus, the energy integral can be done as

$$\begin{aligned} \epsilon_\nu &\sim E_{(A,Z+1)} \frac{\lambda_{(A,Z+1)}}{m_u} \\ &\times \left(e^{\beta(E_{(A,Z+1)} + \Delta_A - \mu_e)} Y_{(A,Z)} f_\nu(E_{(A,Z+1)}) - Y_{(A,Z+1)}\right) \end{aligned} \quad (32)$$

The first and second terms in the r.h.s show the neutrino heating rate of the neutrino absorption by the (A,Z) nucleus and the neutrino loss rate of the electron capture on the $(A,Z+1)$ nucleus, respectively. Finally, considering the change of the number densities of electron and nuclei, the heating (or cooling) rates of the neutrino absorption and the electron capture are estimated as

$$\begin{aligned} \epsilon_{\text{abs}} &\sim (E_{(A,Z+1)} + \Delta_A - \mu_e) \frac{\lambda_{(A,Z+1)}}{m_u} \\ &\times e^{\beta(E_{(A,Z+1)} + \Delta_A - \mu_e)} Y_{(A,Z)} f_\nu(E_{(A,Z+1)}) \end{aligned} \quad (34)$$

$$\epsilon_{\text{emt}} \sim -(E_{(A,Z+1)} + \Delta_A - \mu_e) \frac{\lambda_{(A,Z+1)}}{m_u} Y_{(A,Z+1)}. \quad (35)$$

The two equations show that the inverse process of the electron capture reaction should have a large reaction rate in order for the neutrino absorption to be efficient. Therefore here we examine the absorption reactions by ^{20}O , ^{20}F , ^{24}Ne , and ^{24}Na , which are products of electron captures on ^{20}Ne and ^{24}Mg . Moreover, the heat emitted per one reaction, $E_{(A,Z+1)} + \Delta_A - \mu_e$, should be positive for heating for the neutrino absorption reaction, otherwise it cools surroundings. Due to the large μ_e , $E_{(A,Z+1)} + \Delta_A - \mu_e$ tends to be negative in the whole region of the ONe core. As an exception in the considered reactions, the energy term can be positive in the outer region of $M_b > 0.4 M_\odot$. This is shown in the top panel of Fig. 21, in which the distribution of relevant energies are shown.

Furthermore, in order to have a heating effect, the reaction rate of neutrino absorption should exceed that of the electron capture. Fractions of $e^{\beta(E_\nu + \Delta_A - \mu_e)}$, f_ν , $Y_{20\text{F}}/Y_{20\text{Ne}}$, and their product are shown in the middle

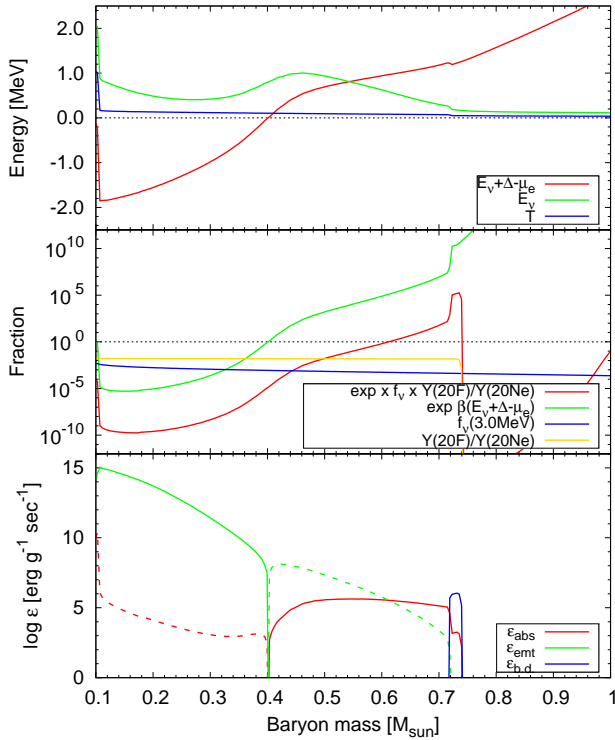


Figure 21. A posteriori estimate of the heating rate of $^{20}\text{F} + \nu_e \rightarrow ^{20}\text{Ne} + e^-$ using model T9.0 with the flame front at $0.1 M_\odot$. Top) distributions of energies related to the reaction. Middle) distributions of fractions related to the reaction. Bottom) distributions of heating rates. Rates of neutrino absorption, electron capture, and beta decay are respectively shown by red, green, and blue lines. Solid lines show the heating rates, while dashed lines show cooling rates.

panel of Fig. 21. Thanks to the positive $E_\nu + \Delta_A - \mu_e$, the exponent exceeds unity in an outer region of $> 0.4 M_\odot$. Because the neutrino distribution function f_ν gives nearly energy-independent value of $\sim 1 \times 10^{-4} - 3 \times 10^{-3}$ for the concerning range of $E_\nu \lesssim 7$ MeV, $f_\nu(3.0 \text{ MeV})$ is shown as a representative case. During the evolutionary stage, non-negligible amount of ^{20}F has been mixed up to the outer region by the convection powered by electron captures on ^{24}Mg and ^{20}Ne . As a result, the convective region has relatively high $Y(^{20}\text{F})/Y(^{20}\text{Ne}) \sim 10^{-2}$. In the end, the fraction $e^{\beta(E_\nu + \Delta_A - \mu_e)} \times f_\nu \times Y_{20\text{F}}/Y_{20\text{Ne}}$ exceeds unity in an outer region of $0.62 - 0.74 M_\odot$.

The heating or cooling rates of the reactions $^{20}\text{F} + \nu_e \rightarrow ^{20}\text{Ne} + e^-$ and $^{20}\text{Ne} + e^- \rightarrow ^{20}\text{F} + \nu_e$ are shown in the bottom panel of Fig. 21. In the innermost region of $M_b < 0.40 M_\odot$ with the high electron chemical potential μ_e , the electron capture reaction has a heating effect and thus shown by the green solid line. The heating rate is much larger than the cooling rate of the neutrino absorption reaction, which is shown by the red dashed line.

Meanwhile, in the middle region of $0.40 M_\odot < M_b < 0.72 M_\odot$, the electron capture reaction has a cooling effect and the neutrino absorption reaction has a heating effect. The heating rate, shown by the red solid line, exceeds the cooling rate, shown by the green dashed line, in the region of $0.62 M_\odot < M_b < 0.72 M_\odot$. Besides, in the outermost region of $0.72 M_\odot < M_b < 0.74 M_\odot$, the heating rate of the beta decay of $^{20}\text{F} \rightarrow ^{20}\text{Ne} + e^- + \bar{\nu}_e$, which is estimated as $\epsilon_{\text{b.d.}} \sim (E_\nu + \Delta_A - \mu_e)(\lambda_{\text{b.d.}}/m_u)Y_{20\text{F}}$, becomes larger than the neutrino absorption reaction (the blue solid line). In summary, although the neutrino absorption reaction has a heating effect only in the narrow region of $0.62 M_\odot < M_b < 0.72 M_\odot$, the weak reactions of the isotopes with the mass number of 20 in total have a net heating effect in the wide regions of $M_b < 0.40 M_\odot$ and $0.62 M_\odot < M_b < 0.74 M_\odot$ in the ONe core.

However, none of them exceeds the heating rate of neutrino-electron scattering, which reaches $\epsilon_{\text{esc}} \sim 3 \times 10^{17} \text{ erg g}^{-1} \text{ sec}^{-1}$ at the flame front. Similar to ^{20}F - ^{20}O , other nuclei can also have heating effects mainly by the electron capture reactions in the innermost region, but these rates are merely $\lesssim 1 \times 10^{15} \text{ erg g}^{-1} \text{ sec}^{-1}$ and much weaker than the neutrino-electron scattering. Therefore we conclude that neither neutrino absorption nor electron capture on nuclei effectively enhance the flame propagation in the ONe core.

6.2. Propagation velocity of conductive flame with corrugated fronts

The conductive flame velocity may be enhanced due to the corrugation effect by turbulence. In this subsection, we try to compare the flame propagation velocity obtained in this work to the velocity of conductive flame with corrugated flame fronts.

As a result of the runaway oxygen+neon burning, the entropy and the temperature of the matter increase, and accordingly the density decreases to keep the pressure nearly constant. This makes a density inversion at the flame front, providing a satisfactory condition for the Rayleigh-Taylor (RT) instability. Under this instability, a large-scale convective flow may be developed. Small-scale turbulence is also possibly driven by the RT instability, or it appears as a result of the turbulent cascade, in which the Kelvin-Helmholtz instability plays an important role. The burning front can be corrugated by the turbulence, increasing the surface area of the fuel/ash boundary layer. As a result, the net consumption rate of the nuclear fuel as well as the effective propagation velocity is enhanced.

Considering the scale-invariant property in the turbulent front propagation, Pocheau (1994) has derived a general relation between the effective flame propagation

velocity in a large scale, U_T , the laminar flame velocity in a small scale, U_N , and the turbulence intensity, U' , as

$$U_T^\alpha = U_N^\alpha + \beta U'^\alpha. \quad (36)$$

For the two constants, $\alpha = 2$ is derived by imposing the energy conservation, and $\beta = 4/3$ is implied to be consistent with a numerical simulation (Peters 1999; Schmidt et al. 2006). For U_N , V_{cond} by Timmes & Woosley (1992),

$$V_{\text{cond}} = 5.18 \times 10^6 \left(\frac{\rho}{6 \times 10^9} \right)^{1.06} \left(\frac{X(^{16}\text{O})}{0.6} \right)^{0.688} \text{ cm se} \quad (37)$$

is applied. For U' , we tentatively apply the Sharp-Wheeler relation (Davies & Taylor 1950; Sharp 1984)

$$U' = V_{\text{RT}}(l) \quad (38)$$

$$= 0.5 \sqrt{lg_{\text{eff}}}, \quad (39)$$

where $g_{\text{eff}} \equiv (\Delta\rho/\rho)g$ is the buoyancy force of the convective blob formed at the flame front and $l = r_f$, assuming the turbulence is mostly driven by the RT instability. In the end, the effective flame velocity is estimated as $V_{\text{eff}} = \sqrt{V_{\text{cond}}^2 + 4V_{\text{RT}}^2/3}$.

The time evolution of the related velocities are shown in Fig. 22 for models of T9.0, T9.0ye, and N8.8 by the top, middle, and bottom panels respectively. For all models, $V_{\text{eff}} \approx \sqrt{4/3}V_{\text{RT}}$ since $V_{\text{cond}} \ll V_{\text{RT}}$. In the model T9.0, the conductive energy transport will have a negligible contribution to the flame propagation, as always $V_{\text{eff}} < V_{\text{prop}}$. The same can be found for the model N8.8 and for the later propagation of $t_{\text{pb}} > \sim -0.15$ sec in the model T9.0ye. On the other hand, V_{eff} is comparable to V_{prop} in the early phase of $t_{\text{pb}} < \sim -0.15$ sec in the model T9.0ye, in which the flame propagation is mainly powered by the neutrino-electron scattering.

The conductive energy transport possibly helps the flame propagation in the early phase of an ONe core, if the core is initially hydrostatic. Therefore it is important to determine how the ONe core is hydrostatically stable at the onset of the central O+Ne ignition. The model T9.0 seems to be destabilized due to the remapping procedure from the stellar evolution code to the hydrodynamic code, and the model T9.0ye is the other extreme case in which the hydrostatic stability is artificially posed. The real ONe core, if it exists, would have a gravitationally-stable state in between the two models. Because only a very simple estimate has been done here, it will be interesting to investigate how conductive burning front propagates through the hydrostatic ONe medium by a 3D simulation even for the case with the high ignition density.

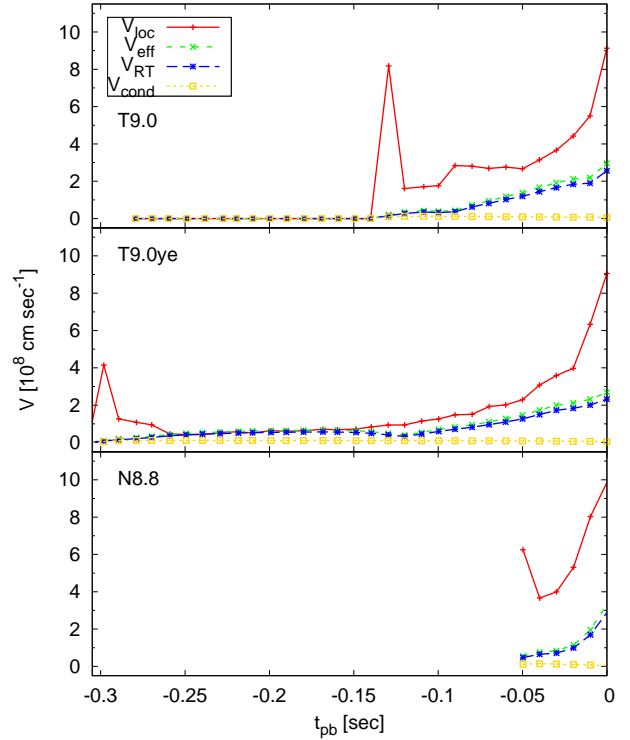


Figure 22. The time evolution of the propagation velocities is shown for models of T9.0 (top), T9.0ye (middle), and N8.8 (bottom). Velocities are the flame propagation velocity obtained in this work (V_{prop} , red, solid), the effective propagation velocity of conductive flame (V_{eff} , green, short-dashed), the turbulence intensity (V_{RT} , blue, long-dashed), and the laminar conductive flame velocity (V_{cond} , yellow, dotted), respectively, and are calculated every 0.01 sec before the core bounce.

One missing argument here is the effect of density increase by the electron capture reaction. The electron capture reaction by free protons that initiates immediately after the flame front passes the region has a short timescale of ~ 0.01 sec. It decreases Y_e from ~ 0.5 to $\lesssim 0.4$, so that causes the density increase of $\sim 25\%$. However, the timescale of the flame propagation, τ_{flame} , is ~ 0.1 sec, and the extent of the density inversion due to the oxygen+neon burning is merely $\Delta\rho/\rho \lesssim 0.1$. Therefore, the region just below the flame front will be rapidly stabilized by the electron capture reaction. In order to estimate the turbulent intensity more accurately, the effect of the rapid stabilization should be properly taken into consideration.

7. CONCLUSION

A critical mass ONe core with a high ignition density of $\rho_{\text{ign}} \gtrsim 9 \times 10^{10} \text{ g cm}^{-3}$ is considered to be destined to gravitational collapse to form a neutron star. Whereas a number of works have been performed to investigate

phases of the super-AGB star evolution and the ECSN explosion, the final core evolution from the central ONe ignition towards core bounce has not been investigated in detail so far. This is because the ONe core consists of combustible elements so that one has to follow a complex phase transition from the O+Ne composition into the NSE state. Thus, we have simulated the late core evolution using a neutrino-radiation-hydrodynamic code, which treats not only neutrino reactions by solving the elaborate Boltzmann equation but also the nuclear burning and electron capture reactions. Special care is also taken to remap the initial structure as consistent with the original evolution calculation as possible.

We have observed that the late core evolution is affected by complex interplay among the nuclear reactions, the structure evolution, and the flame propagation. First, the oxygen+neon burning leads to (i) heating by the release of the rest mass energy; (ii) Y_e reduction due to accompanying electron capture reactions by free protons down to $Y_e \sim 0.36$, and even further by NSE heavy nuclei; and (iii) energy reduction due to ν_e emission by the electron capture. In addition, we have pointed out that (iv) reduction in γ due to photo-disintegration in the NSE region results from the oxygen+neon burning. As a consequence, the core becomes more and more unstable as the flame propagation extends the central NSE region. Moreover, the fast electron captures caused by the oxygen+neon burning result in (v) the intense ν_e radiation with the luminosity of $L_{\nu_e} \gtrsim 10^{51}$ erg s⁻¹ even before the core bounce.

Second, owing to the destabilization described above and to the intrinsically unstable core structure due to the soft EOS with $\gamma \sim 4/3$, the ONe core starts to contract after the central ignition. Thus the temperature rise due to the compression has a major contribution to trigger the succeeding nuclear burning ahead of the flame front. Furthermore, we have found that the intense pre-bounce ν_e radiation heats the broad cold region of the ONe core by neutrino-electron scattering, which acts as a new driving mechanism of the flame propagation in the collapsing ONe core. The resulting heating rate can be as high as $\sim 3 \times 10^{17}$ erg g⁻¹ sec⁻¹ and much more efficient than any other neutrino reactions and electron capture reactions. In summary, the flame propagation in the collapsing ONe core is driven by both adiabatic compression and heating by neutrino-electron scattering.

Comparison of results of the progenitor model T9.0 and the artificially stabilized model T9.0ye shows that the different degree of the initial hydrostatic/dynamical stability affects the flame propagation velocity in the early phase of $t_{\text{pb}} \lesssim -0.05$ sec. The early flame veloc-

ity is $\sim 1 \times 10^8$ cm sec⁻¹ in the nearly hydrostatic core of model T9.0ye. On the other hand, faster velocity of $\sim 3 \times 10^8$ cm sec⁻¹ is obtained for model T9.0, because the faster core contraction enhances the adiabatic compression and besides the fast propagation velocity results in more efficient neutrino heating. Having different propagation velocities in the early phases, models with different degree of the initial hydrostatic stability have different durations from the ignition until core bounce. The durations of the pre-bounce phases are 0.13 sec for the model T9.0 and 0.30 sec for the model T9.0ye, respectively. We note that the obtained flame velocity of $\sim 10^8$ cm sec⁻¹ is more than one-order-of-magnitude faster than the estimated laminar flame velocity driven by heat conduction, which has been considered as the main driving mechanism of the flame propagation in the ONe core.

Kato et al. (2017) have simulated the observability of neutrinos that are emitted during the pre-bounce phases for progenitors of an ECSN and FeCCSNe. They have found that a progenitor of an ECSN can be observationally distinguishable from a progenitor of a FeCCSN based on the detection and non-detection of ν_e and $\bar{\nu}_e$, if the progenitor star locates close to the earth of ~ 200 pc. Besides, we predict that the duration of the pre-bounce neutrino emission phase can be determined by observing the pre-supernova neutrinos since the luminosity of ν_e is large from the beginning. We have shown that this duration strongly depends on the different initial structures having the different degree of the core hydrostatic stability. Therefore, detection of pre-supernova neutrinos has a potential importance to constrain the initial core hydrostatic-stability state.

In spite of the different propagation in the early phase, the core evolution in the late phase of $t_{\text{pb}} \gtrsim -0.05$ sec becomes similar for models of T9.0 and T9.0ye. The model N8.8 develops a more compact central NSE region during the whole collapsing phase. As a result, the flame front in the model N8.8 is mostly driven by heating of neutrino-electron scattering, which qualitatively differs from models T9.0 and T9.0ye. However, important characteristics such as time evolutions of the central density and the neutrino luminosities still show striking resemblance to each other. In the end, successful explosions take place for both the models T9.0 and N8.8. This indicates that the late dynamical evolution of $t_{\text{pb}} \gtrsim -0.05$ sec of the critical mass ONe core is unique and independent from the outer flame propagation. We are currently working to follow the further explosion as an ECSN of these models, in order to determine their explosion properties, such as the explosion energies and the remnant masses. Results will be reported in the

near future.

We acknowledge invaluable comments from the anonymous referee that help to improve the manuscript. Authors appreciate Ken'ichi Nomoto for providing us the progenitor model N8.8. We thank Andrius Juodagalvis and Shun Furusawa for providing electron capture rates for NSE compositions. We also thank Chinami Kato for fruitful discussions about neutrino reactions and Jonathan Mackey for careful reading of the draft. K.T. was supported by the Japan Society for the Promotion of Science (JSPS) Overseas Research Fellowships. This work was supported by Grant-in-Aid for Scientific Research (26104006, 15K05093, 17H01130, 17K05380) and Grant-in-Aid for Scientific Research on

Innovative areas "Gravitational wave physics and astronomy:Genesis" (17H06357, 17H06365) from the Ministry of Education, Culture, Sports, Science and Technology (MEXT), Japan. For providing high performance computing resources, Computing Research Center, KEK, JLDG on SINET4 of NII, Research Center for Nuclear Physics, Osaka University, Yukawa Institute of Theoretical Physics, Kyoto University, and Information Technology Center, University of Tokyo are acknowledged. This work was partly supported by research programs at K-computer of the RIKEN AICS, HPCI Strategic Program of Japanese MEXT, Priority Issue on Post-K computer (Elucidation of the Fundamental Laws and Evolution of the Universe) and Joint Institute for Computational Fundamental Sciences (JICFus).

REFERENCES

- Arnett, W. D. 1977, *ApJS*, 35, 145
- Böhm-Vitense, E. 1958, *ZA*, 46, 108
- Braaten, E., & Segel, D. 1993, *PhRvD*, 48, 1478
- Bruenn, S. W. 1985, *ApJS*, 58, 771
- Bruenn, S. W., & Haxton, W. C. 1991, *ApJ*, 376, 678
- Canal, R., Isern, J., & Labay, J. 1992, *ApJL*, 398, L49
- Chandrasekhar, S. 1939, *An introduction to the study of stellar structure*
- Chechetkin, V. M., Eramzhyan, R. A., Folomeshkin, V. N., et al. 1976, *Physics Letters B*, 62, 100
- Chechetkin, V. M., Gershtein, S. S., Imshennik, V. S., Ivanova, L. N., & Khlopov, M. I. 1980, *Ap&SS*, 67, 61
- Davies, R. M., & Taylor, G. 1950, *Proceedings of the Royal Society of London Series A*, 200, 375
- Dessart, L., Burrows, A., Ott, C. D., et al. 2006, *ApJ*, 644, 1063
- Doherty, C. L., Gil-Pons, P., Siess, L., & Lattanzio, J. C. 2017, *PASA*, 34, e056
- Doherty, C. L., Siess, L., Lattanzio, J. C., & Gil-Pons, P. 2010, *MNRAS*, 401, 1453
- Dzhioev, A. A., Vdovin, A. I., Ponomarev, V. Y., & Wambach, J. 2011, *Physics of Atomic Nuclei*, 74, 1162
- Dzhioev, A. A., Vdovin, A. I., Wambach, J., & Ponomarev, V. Y. 2014, *PhRvC*, 89, 035805
- Fischer, T., Whitehouse, S. C., Mezzacappa, A., Thielemann, F.-K., & Liebendörfer, M. 2010, *A&A*, 517, A80
- Friman, B. L., & Maxwell, O. V. 1979, *ApJ*, 232, 541
- Furusawa, S., Nagakura, H., Sumiyoshi, K., Kato, C., & Yamada, S. 2017a, *PhRvC*, 95, 025809
- Furusawa, S., Sumiyoshi, K., Yamada, S., & Suzuki, H. 2017b, *Nuclear Physics A*, 957, 188
- Garcia-Berro, E., & Iben, I. 1994, *ApJ*, 434, 306
- Gutierrez, J., Garcia-Berro, E., Iben, Jr., I., et al. 1996, *ApJ*, 459, 701
- Herwig, F. 2000, *A&A*, 360, 952
- Hillebrandt, W., Nomoto, K., & Wolff, R. G. 1984, *A&A*, 133, 175
- Iben, Jr., I., Ritossa, C., & Garcia-Berro, E. 1997, *ApJ*, 489, 772
- Isern, J., Canal, R., & Labay, J. 1991, *ApJL*, 372, L83
- Janka, H.-T. 2012, *Annual Review of Nuclear and Particle Science*, 62, 407
- Janka, H.-T., Müller, B., Kitaura, F. S., & Buras, R. 2008, *A&A*, 485, 199
- Jones, S., Röpke, F. K., Pakmor, R., et al. 2016, *A&A*, 593, A72
- Jones, S., Hirschi, R., Nomoto, K., et al. 2013, *ApJ*, 772, 150
- Juodagalvis, A., Langanke, K., Hix, W. R., Martínez-Pinedo, G., & Sampaio, J. M. 2010, *Nuclear Physics A*, 848, 454
- Juodagalvis, A., Langanke, K., Martínez-Pinedo, G., et al. 2005, *Nuclear Physics A*, 747, 87
- Kato, C., Nagakura, H., Furusawa, S., et al. 2017, *ApJ*, 848, 48
- Kippenhahn, R., & Weigert, A. 1990, *Stellar Structure and Evolution*
- Kitaura, F. S., Janka, H.-T., & Hillebrandt, W. 2006, *A&A*, 450, 345
- Langanke, K., Martínez-Pinedo, G., Müller, B., et al. 2008, *Physical Review Letters*, 100, 011101
- Langer, N. 2012, *ARA&A*, 50, 107
- Lau, H. H. B., Gil-Pons, P., Doherty, C., & Lattanzio, J. 2012, *A&A*, 542, A1

- Leung, S.-C., & Nomoto, K. 2017, *Mem. Soc. Astron. Italiana*, 88, 266
- Maxwell, O. V. 1987, *ApJ*, 316, 691
- Mayle, R., & Wilson, J. R. 1988, *ApJ*, 334, 909
- Melson, T., Janka, H.-T., & Marek, A. 2015, *ApJL*, 801, L24
- Mezzacappa, A., & Bruenn, S. W. 1993, *ApJ*, 410, 740
- Miyaji, S., & Nomoto, K. 1987, *ApJ*, 318, 307
- Miyaji, S., Nomoto, K., Yokoi, K., & Sugimoto, D. 1980, *PASJ*, 32, 303
- Nakazato, K., Sumiyoshi, K., Suzuki, H., et al. 2013, *ApJS*, 205, 2
- Nakazato, K., Sumiyoshi, K., & Yamada, S. 2007, *ApJ*, 666, 1140
- Nomoto, K. 1984, *ApJ*, 277, 791
- . 1987, *ApJ*, 322, 206
- Nomoto, K., & Kondo, Y. 1991, *ApJL*, 367, L19
- Nomoto, K., Sugimoto, D., & Neo, S. 1976, *Ap&SS*, 39, L37
- Oda, T., Hino, M., Muto, K., Takahara, M., & Sato, K. 1994, *Atomic Data and Nuclear Data Tables*, 56, 231
- Patton, K. M., Lunardini, C., Farmer, R. J., & Timmes, F. X. 2017, *ApJ*, 851, 6
- Peters, N. 1999, *Journal of Fluid Mechanics*, 384, 107
- Pocheau, A. 1994, *PhRvE*, 49, 1109
- Poelarends, A. J. T., Herwig, F., Langer, N., & Heger, A. 2008, *ApJ*, 675, 614
- Radice, D., Burrows, A., Vartanyan, D., Skinner, M. A., & Dolence, J. C. 2017, *ApJ*, 850, 43
- Ritossa, C., Garcia-Berro, E., & Iben, Jr., I. 1996, *ApJ*, 460, 489
- Sampaio, J. M., Langanke, K., Martínez-Pinedo, G., & Dean, D. J. 2002, *Physics Letters B*, 529, 19
- Schmidt, W., Niemeyer, J. C., Hillebrandt, W., & Röpke, F. K. 2006, *A&A*, 450, 283
- Schwab, J., Quataert, E., & Bildsten, L. 2015, *MNRAS*, 453, 1910
- Shapiro, S. L., & Teukolsky, S. A. 1986, *Black Holes, White Dwarfs and Neutron Stars: The Physics of Compact Objects*, 672
- Sharp, D. H. 1984, *Physica D Nonlinear Phenomena*, 12, 3
- Shen, H., Toki, H., Oyamatsu, K., & Sumiyoshi, K. 1998, *Nuclear Physics A*, 637, 435
- Siess, L. 2006, *A&A*, 448, 717
- . 2010, *A&A*, 512, A10
- Spruit, H. C. 1992, *A&A*, 253, 131
- Sugimoto, D., & Fujimoto, M. Y. 2000, *ApJ*, 538, 837
- Sumiyoshi, K., Yamada, S., & Suzuki, H. 2007, *ApJ*, 667, 382
- . 2008, *ApJ*, 688, 1176
- Sumiyoshi, K., Yamada, S., Suzuki, H., et al. 2005, *ApJ*, 629, 922
- Suzuki, T., Toki, H., & Nomoto, K. 2016, *The Astrophysical Journal*, 817, 163
- Takahashi, K., Umeda, H., & Yoshida, T. 2014, *ApJ*, 794, 40
- Takahashi, K., Yoshida, T., & Umeda, H. 2013, *ApJ*, 771, 28
- Takahashi, K., Yoshida, T., Umeda, H., Sumiyoshi, K., & Yamada, S. 2016, *MNRAS*, 456, 1320
- Timmes, F. X., & Woosley, S. E. 1992, *ApJ*, 396, 649
- Umeda, H., & Nomoto, K. 2008, *ApJ*, 673, 1014
- Umeda, H., Nomoto, K., Yamaoka, H., & Wanajo, S. 1999, *ApJ*, 513, 861
- Unno, W. 1967, *PASJ*, 19, 140
- Ventura, P., & D'Antona, F. 2005, *A&A*, 431, 279
- Weaver, T. A., Zimmerman, G. B., & Woosley, S. E. 1978, *ApJ*, 225, 1021
- Yamada, S. 1997, *ApJ*, 475, 720
- Yamada, S., Janka, H.-T., & Suzuki, H. 1999, *A&A*, 344, 533

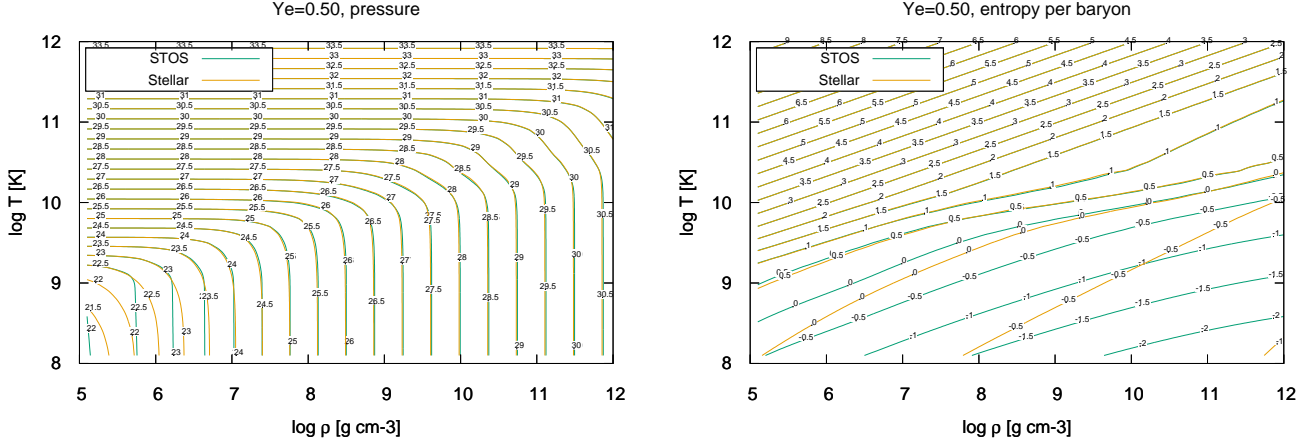


Figure 23. Comparisons of pressure (left) and entropy per baryon (right) between the STOS and the stellar EOSs in density-temperature planes. Contours of the thermodynamic quantities are shown by lines. Attaching numbers show log values of pressure (in erg cm^{-3}) or entropy per baryon (in units of the Boltzmann constant k_B). Green lines are STOS EOS results, while orange lines are results of the stellar EOS.

APPENDIX

A. EOS COMPARISON

In Fig. 23, pressure and entropy per baryon calculated by the two EOSs are shown for the case of $Y_e = 0.5$. The NSE composition determined by the STOS EOS is used for the input of the stellar EOS in this case. Pressure well matches for $T > 10^9$ K, if Y_e is less than 0.56. The STOS pressure will be unreliable below this temperature or above this Y_e , since the original table has data points only at $T = 0$ K and $Y_e = 10^{-0.25}$. For entropy per baryon, s_k , both EOSs provide almost the same values for wide range of Y_e , if $s_k > 3 k_B$ or $T > 10^{9.7}$ K. A large part of the disagreement seen at low entropy region of $s_k < 1 k_B$ is explained by omission of the entropy of heavy nuclei in the STOS EOS. Since matters in a such region are always covered by the stellar EOS, this omission does not affect our calculation.

B. AN IMPROVED GRID RECONSTRUCTION METHOD

A frequency function $f(r)$ and an integrated frequency function $F(r) = \int_{\text{center}}^r f(r') d \ln r'$ are defined. Grid points are determined to be evenly spaced in terms of the integrate frequency function. Thus a radius interval between two grid points becomes

$$\Delta \ln r \simeq \frac{d \ln r}{dF} \Delta F \quad (\text{B1})$$

$$= f^{-1} \Delta F, \quad (\text{B2})$$

so that we named the function $f(r)$ as the frequency function. As for the actual frequency function,

$$f = \begin{cases} C 4\pi r^3 \rho (P > 10^{20} \text{ erg cm}^{-3}) \\ \frac{|d \log P|}{|d \log r|} \text{ (otherwise),} \end{cases} \quad (\text{B3})$$

where C is a constant, is used.